1993

A model system for the study of chromized coatings

Vishal Agarwal
Lehigh University

AUTHOR:

Agarwal, Vishal

TITLE:

A Model System for the Study of Chromized Coatings

DATE: October 10, 1993

A Model System for the Study of Chromized Coatings

by

Vishal Agarwal

A Thesis

Presented to the Graduate Committee

of Lehigh University

in Candidacy for the Degree of

Master of Science

in

Materials Science and Engineering

July 1993

Certificate of Approval

This thesis is accepted and approved in partial fulfillment of the requirements for the degree of Master of Science.

7/23/93
Date

Professor in charge

Chairman of the
Department of Materials
Science & Engineering

ACKNOWLEDGEMENTS

I would like to thank my advisor Dr. Marder, for his guidance, support and encouragement throughout this project. I gratefully acknowledge his contribution to the completion of this thesis. I would also like to thank Dr. Goldstein for his valuable comments and suggestions. I am indebted to Mr. A.O. Benscoter for his metallographic assistance.

I would like to acknowledge all fellow students who have helped to make my stay at Lehigh an enjoyable one. I would like to especially thank Brian J. Smith. His comments were always useful and the discussions (academic and non-academic) very enjoyable. I would also like to thank the consortium of utility companies for their funding of this project.

Finally, I would like to thank my parents and my brother who provided me love and motivation in all my efforts.

TABLE OF CONTENTS

LIST OF TABLES

LIST OF FIGURES

ABSTRACT

The processing-microstructure relationships of the chromized coatings have been investigated with the help of a model system. In the model system, an electrodeposition technique was used to deposit the chromium layer on top of a high purity Fe-C alloy (0.2%C). Microcracks were present in the chromium layer due to the plating conditions. A decarburized layer was introduced below the Cr layer to simulate the conditions in the utility boiler tube coatings. Diffusion studies at 600^{0}C were conducted to investigate the effect of grain shape (columnar vs equiaxed) and the ferritic microstructure on the diffusion of carbon in the decarburized layer. Diffusion studies were also conducted at 1000^{0}C to study the effect of austenitic microstructure on the diffusion of carbon and to simulate the chromized coating formation mechanism. Quench tests were done to study the effect of cooling rates on the microstructure formation at 1000^{0}C. Tests were also done to study the behavior of microcracks in the electrodeposited Cr in high temperature oxidation and sulphidation environments. The testing included isothermal exposure at 600^{0}C in air and pure SO_2 gaseous environments.

It was found that the grain shape i.e. columnar or equiaxed does not have any effect on the diffusion of carbon at 600^{0}C. There was no significant change in the needle like precipitate morphology or the grain boundary carbides in the columnar or equiaxed samples after the heat-treatment. Diffusion studies in the ferritic microstructure at 600^{0}C led to the formation of a reaction layer below the chromium layer. The thickness of this reaction layer increases with time in a parabolic manner. The reaction layer consists of two layers. Quantitative

analysis and backscattered images of the reaction layer indicates the possibility of one of the layers to be a carbide layer. Electron probe analysis indicated the carbon content in this layer to be high enough (nearly 5 wt%) to form a carbide layer. The other layer may be a solid solution of Fe, Cr and carbon or it may contain fine carbide precipitates in a ferrite matrix.

The high solubility of carbon in austenite was found to be responsible for large carbon poisoning in the chromized coatings. A microstructure similar to the typical chromized microstructure was obtained using chromium electrodeposition and subsequent heat-treatment (at 1000^0C) and slow cooling technique. The chromized coating microstructure (voids, carbides etc.) formed only on slow furnace cooling. Thermal cycle above the eutectoid temperature is an important factor in chromized microstructure formation. The absence of voids in the coating on fast cooling indicated that they perhaps formed due to a vacancy-interstitial interaction.

The microcracks in the electodeposited Cr layer were found to be attacked in oxidation and sulphidation environments. The microcrack size and area fraction also increased during the high temperature heat-treatment. The kinetics of oxidation and sulphidation attack at the microcracks followed a logarithmic relationship. The increase in size and area-fraction of the microcracks can be attributed to the formation of a corrosion product (possibly chromium oxide) in the microcracks. The logarithmic kinetics of attack indicates that the corrosion product inside the microcracks limits further attack. The thermal stresses generated during the heat-treatment (due to the differential thermal expansion between Cr and Fe) can also lead to a change in the microcrack morphology.

I. INTRODUCTION

Metals and alloys which are used for high temperature applications are most often subject to various corrosion mechanisms. This has been costly for many industries [1], and in the response, many types of coatings have been developed and applied to metallic surfaces for corrosion resistance. Of the types of coatings tried, diffusion coatings have been the most successful and most widely used in many high temperature, corrosive environment applications. A diffusion coating is the result of any process whereby a metal or alloy is either: (1) Coated with another metal or alloy and heated to a sufficient temperature in a suitable environment, or (2) exposed to a solid solution of the metal or alloy to be coated at a suitable temperature. This causes diffusion of the metal or alloy being coated into the substrate thus forming a coating with resultant changes in the composition and properties of the substrate [2].

Chromizing, the process of coating a substrate metal/alloy with chromium, is a popular means for high temperature surface protection. The coating is formed by diffusing chromium atoms into a metal substrate which produces an alloy layer that is an integral part of the substrate [3]. The coating process involves packing the steel in a powder mixture which contains a chromium source (pure chromium or ferrochrome), an inert filler (usually alumina) and a halide activator (NH_4Cl, NH_4I etc.). The pack is heated in dry inert gas or hydrogen for 10-12 hours at 1000-1300^{0}C to form coatings in the range of 2-5mm thick. The coating is immune to flaking and spallation problems which affect plating, overlay and spray coatings [4].

The coating (figure I.1) is characterized by a thin chromium carbide layer (not visible in low magnification figure I.1) under the outer chromium layer (marked Cr). There is a diffusion zone below the carbide layer in which the Cr concentration decreases from 30-50 wt% beneath the carbide case to about 10 wt% at the coating/substrate interface (marked I). Chromium carbides are present in the columnar grain boundaries (marked c), often as large particles. A decarburized zone (marked decarb) is present in the steel just below the coating and is believed to be the source of carbon from which the outer case and carbide particles in the coating are formed [5-8]. Coatings formed on carbon steel often contain a substantial amount of porosity and random large voids (marked v) near the coating surface just below the outer layer [9]. These pores and voids can lead to internal oxidation attack, as well as crack initiation in the coating during service. The columnar grains and the grain boundary carbides are harmful from the point of view of mechanical properties. Service exposed coatings frequently fail along the columnar grain boundary carbides [10].

Thus, various features in the microstructure of chromized coatings such as porosity, voids, columnar grains and grain boundary carbides are harmful to coating performance. A control of these can greatly enhance the coating performance.

The purpose of this research effort is to investigate the processing-microstructure relationships of the chromized coatings with the help of a model system. In the model system, electrodeposited chromium was used as the chromium source instead of using the conventional pack method. The main objectives of this research work were: To study the effect of grain shape (columnar vs equiaxed) on

the diffusion of carbon, to study the effect of microstructure (ferrite vs austenite) on the diffusion of carbon and carbide formation, and to simulate the chromizing procedure.

II. LITERATURE REVIEW

An understanding of the phase diagrams in the Fe-Cr-C system is necessary to understand the microstructural interactions in the chromized coatings. Hence, a literature review of the phase relationships in the binary Fe-C, Fe-Cr and Cr-C systems and the ternary Fe-Cr-C system was conducted. An attempt was made to study the various carbide phase equilibria and the diffusion in the ternary Fe-Cr-C system.

II.a Elements

Fe:

Iron melts at 1536^{0}C. and below its melting point, iron has three allotropes: α-Fe, γ-Fe and δ-Fe. Alpha iron possesses a body centered cubic (bcc) crystal structure while gamma iron has a face centerd cubic (fcc) crystal structure. Gamma iron is present between 911 and 1392^{0}C while alpha iron is found below 911^{0}C. Above 1392^{0}C, delta iron (δ) is present and has a bcc crystal structure. The boiling point of iron is 2870^{0}C and its coefficient of linear expansion is 12 μm/m.K [11]. The extent of solubility of the added elements in bcc or fcc iron determines the phase equilibria of binary and higher systems of iron [12].

Cr:

Cr possesses a bcc crystal structure below its melting temperature. The exact value of the melting temperature of Cr has been difficult to determine, mainly because of its high reactivity. The accepted value [13] places the melting

temperature at a mean value of 1878±22^{0}C. The coefficient of linear expansion of chromium is 6.2 μm/m.K [14].

C:

At room temperature, carbon (graphite) has a hexagonal crystal structure. The melting point of carbon is about 3825^{0}C at which the sublimation of carbon takes place. Another allotropic form of carbon is diamond which has a diamond cubic crystal structure. In this review carbon (graphite) will be referred with a hexagonal crystal structure.

II.b BINARY SYSTEMS

Fe-Cr:

The binary Fe-Cr equilibrium phase diagram [15] is shown in figure II.1. Chromium and bcc iron have complete solubility in one another from each end of the phase diagram between 1400 and 1500^{0}C. The phase diagram shows a minimum in the liquidus at 1510^{0}C and about 18% Cr. The alpha and delta allotropes of Fe unite at over 12% Cr to form a continuous solid solution $\alpha\delta$Fe, which has a bcc crystal structure. The range of the fcc gamma phase is restricted to approximately 12% Cr in the Fe-Cr system. The low temperature equilibria (below 800^{0}C) are governed by the sigma(σ) phase. The sigma phase possesses a bcc crystal structure and is brittle in nature. It forms congruently from $\alpha\delta$Fe at 830^{0}C and 46% Cr.

Fe-C:

The phase diagram given by Hanson and Anderko [16] is shown in figure II.2. The addition of carbon to iron

reduces the melting point of the latter until a peritectic reaction occurs at 1493^{0}C [12]; Liquid (L) + delta iron (δFe) → gamma iron (γ Fe). Gamma iron (fcc) has a wide range of solubility extending to near 2%C at the eutectic temperature. As compared to gamma, the composition ranges of δ Fe and α Fe (both bcc) are only 0.1% or less. Rigourous differential thermal analysis [17] (DTA) revealed small differences from the above figure: a stable eutectic at 1150.5^{0}C and 4.39%C and a metastable eutectic at 1147^{0}C and 4.22%C.

Cr-C:

The binary Cr-C diagram is shown in figure II.3 [18]. Properties of various carbides of chromium are given in table 1. Solid solution of C in Cr extends to 0.32%C up to 1490^{0}C where a eutectic reaction L → (Cr) + $Cr_{23}C_6$ occurs. The peritectic reactions at 1520 and 1780^{0}C result in the formation of $Cr_{23}C_6$ and Cr_7C_3 respectively. Cr_3C_2 forms peritectically at 1895^{0}C by the reaction L + C → Cr_3C_2 and Cr_7C_3 melts congruently at 1765±10^{0}C.

II.c SOLID-SOLID EQUILIBRIA IN THE Fe-Cr-C SYSTEM

Below the solidus, the solid phases α-Fe, γ-Fe, $Cr_{23}C_6$, Cr_7C_3, Cr_3C, Cr_3C_2 and graphite determines the phase relationships. All the carbides of Cr have some solubility for iron where Fe replaces Cr in the crystal lattice. Cementite occurs in Fe-Cr-C system as an equilibrium phase (M_3C), with solubility for Cr (due to chromium as a stabilizing agent). The phase relationships at 1000^{0}C are shown in figure II.4 [19]. Here γ-Fe comes in equilibrium with graphite below 1%C. Woodyatt and Krauss [20] carried

out a thorough analysis of 13 ternary alloys under high purity conditions. Their results are given in table 2 and figure II.5. The data was obtained by X-ray methods and calibrated microprobe analysis of carbides and matrix.

The isothermal sections at 850^{0}C and 700^{0}C [12] are shown in figures II.6 and II.7. Figure II.6 shows the equilibria between the gamma phase and the carbides. Figure II.7 shows the equilibrium between the α phase and the carbides. It was found that Cr replaces Fe in M_3C up to about 18% Cr, $M_{23}C_6$ dissolved up to 35% Fe and M_7C_3 up to 50% Fe. The ferrite in equilibrium with both contained 5.6% Cr. σ phase is shown in this figure giving rise to two three phase equilibria α Fe + σ + $M_{23}C_6$ and (Cr) + σ + $M_{23}C_6$ divided by a two phase area $\sigma + M_{23}C_6$. Solubility of carbon in sigma phase is negligible (less than 0.016% at 600^{0}C in a high purity alloy with 43% Cr). With the addition of carbon to Fe-Cr alloys, the γ loop is moved to higher Cr levels and the α + γ field is widened. Fig. II.8 shows the effect of Cr addition on the temperature and carbon content of the $\gamma \rightarrow \alpha$ + M_3C eutectoid. Considering the addition of Cr to Fe-C alloys, the γ field is constricted, the eutectoid temperature is raised and the carbon content of the eutectoid is lowered.

Summary:

The main features of the solid state isothermal sections have been clarified. Particularly in the Fe-corner where the solid-solubility boundaries of the α-Fe and γ-Fe phases have been established with some precision. It is interesting to observe that the solubility of carbon in bcc phase is very limited, less than 0.1%, yet the primary surface of crystallization of this phase is of wide extent in the C-Cr-Fe system.

II.d DIFFUSION IN THE Fe-Cr-C SYSTEM

Chromium diffusion coatings are applied by the pack cementation process. Chromium is transferred to the steel by means of chromium halogen gas which catalyses the transfer of chromium to the surface. The chromized layer then grows in thickness by the diffusion of chromium inwards and by the diffusion of carbon outwards. Different layers of Cr_7C_3, $Cr_{23}C_6$ and $Cr_2(N,C)$ have been identified [22-24]. The chromizing experiments were done by giving a series of long time heat-treatments at high temperatures($>900^0C$) to carbon steels ranging from 0.2 to 1.65 wt% C. After etching and polishing, the Fe and Cr distribution in the specimens was measured in a microprobe [22-24].

The low carbon steels(0.2% C) showed an inner layer of γ, a very thin layer of M_7C_3 and a thick outer layer of $M_{23}C_6$. The figures for 0.45% C steel and 0.7% C steel (fig. II.9) [25]were different in that the layer of M_7C_3 grew thicker in those. For the 1.65% C steel, a new layer of M_3C(cementite) was found between γ and M_7C_3. Since in these cases the chromium rich carbide layer grew on the side which is closest to the chromium source but away from the carbon source, it was concluded [25] that the dominant diffusion mechanism is the diffusion of carbon through the carbide layer. This conclusion is not affected by the fact that the concentration profiles indicate an appreciable interdiffusion between Cr and Fe [26]. The variation in thickness of carbide layers as functions of the carbon content of the steel are fig. II.10 [26].

Menzies and Mortimer [27] studied the influence of

heat-treatment time and temperature and carbon content on the coating thickness. The thickness of the coatings in all materials increased with increasing temperature and duration of treatment. At any one temperature, the thickness after some initial interval of time increases with time in a parabolic manner. This parabolic growth strongly supports the assumption of a diffusion controlled growth rate. The results also indicate that under similar chromizing conditions the thickness of the coating decreases with increasing carbon content of the steel. The concentration of the carbide which appears in the coatings is proportional to the carbon concentration in the steel. Since diffusion through a carbide is slower than in a metal [27], the decreasing coating thickness with increasing carbon content was justified.

Fig.II.11 shows the isothermal section of Fe-Cr-C phase diagram at 1000^0C. The dashed line shows the possible variation of the composition through the chromized layer in alloy steels [25]. Tie lines(dashed) indicate the composition of various phases in equilibria and were found to be in good agreement with the experimental information. The outer surface of the alloy and pure Cr were not found to be in equilibrium as hardly any α was found experimentally at low carbon contents. The exact condition on the outer layer of $M_{23}C_6$ is still not clear since electron microprobe measurements indicated that the Fe content did not go to zero there. This implies that there was appreciable interdiffusion of Fe and Cr [26].

The growth of carbide layers in the ternary Fe-Cr-C system seems to take place under local equilibrium at the interfaces between the various carbide layers. The growth rate depends highly on the driving force for diffusion and the driving force may be the difference in carbon activity

between various phases if carbon diffusion is assumed to be the dominant diffusion mechanism. Thus, here it can be seen that the driving force for diffusion will be different for steels with different carbon composition and hence the formation of carbide layers will be highly dependent on the substrate composition.

Summary

Diffusion in the Fe-Cr-C system has been clarified in terms of various carbide layer formation. The variation of carbide layer formation with the carbon content has been shown. The parabolic growth of chromized coatings strongly supports the assumption of diffusion controlled growth rates.

III. EXPERIMENTAL APPROACH

One of the main purposes of this study is to simulate the diffusion processes occuring in the boiler tubes during operation. Hence isothermal heat-treatments were done at 600^0C which is the upper limit to the temperature at which the boiler tubes operate. Columnar and equiaxed grains in the decarburized layer were obtained to isolate the effects of grain shape on the diffusion of carbon. Diffusion studies in the ferritic (600^0C) and austenitic (1000^0C) regions were done to see the effect of microstructure on the diffusion of carbon. At 1000^0C diffusion studies were conducted to gain an understanding of the chromized coating microstructure formation mechanism.

III.a Decarburization:

Samples of high purity alloy (composition is shown in table 3 [28]) were used in the experimental work. The specimens were cut flat to an approximate size of 30mm in length, 15mm in width and 4mm in thickness. Each sample was ground on 120 grit to remove any oxide film before the heat treatment. The samples were placed in a Lindburg tube furnace equipped with a 2.5" diameter alumina tube. The apparatus is schematically shown in figure III.1. The gas mixture used for decarburization [29] was $18\%H_2$-$82\%N_2$ (dew point 72^0F). The gas mixture was bubbled through water before it entered the furnace and was burned by mixing it with natural gas at the exit. The gas flow rate was kept approximately at 600 ml/minute. The tube furnace was purged with nitrogen for two hours prior to the start of gas mixture flow.

Decarburization in the two phase ferrite plus

austenite region at 815^{0}C for two hours produced a decarburized columnar structure to an average depth of 500μm (fig. III.2a). To obtain decarburized equiaxed grains (fig. III.3a), these samples were heated in the fully austenitic region at 925^{0}C for 10 minutes to induce the $\alpha \rightarrow \gamma$ transformation. Figures III.2b and III.2c show needle like precipitates in the decarburized columnar layer after the decarburization heat-treatment. These needle like precipitates were also seen in the decarburized equiaxed samples (figs. III.3b and III.3c). A number of etchants were tried on these precipitates. 4% picral etched these precipitates indicating that they may be carbides, nitrides or carbonitrides. Modified Murakami's reagent did not etch these precipitates [30] indicating that these needles may be nitrides or carbonitrides (modified murakami's reagent etches carbides but does not etch nitrides or carbonitrides). No other techniques were used to obtain composition of these needles. In figures III.2c and III.3c these needle like precipitates can be clearly seen at higher magnification. The samples were furnace cooled in all the treatments.

III.b Electroplating:

Both the equiaxed and columnar decarburized samples were then electroplated with chromium (figs. III.4 and III.5) using electrodeposition technique. This technique is convenient and cheaper as compared to the pack cementation technique for chromium deposition onto the substrate. The samples were cleaned before plating by mechanically grinding them to 600 grit followed by mechanical polishing on 6μm diamond, degreasing in acetone and then rinsing in cold water. Non-conductive paint was applied to the non-decarburized surface of the samples so

that the electrodeposition occurs only on the surface that was decarburized. The plating bath contained 300 gm/litre Cr_2O_3, 2.5 gm/litre H_2SO_4 and 4.5 gm/litre sodium florosilicate to act as an activator. All the deposits were produced using a bath temperature of 55^0C, a current density of 4000 amp/m^2 and a plating time of 35 minutes. A Pb rod was used as the anode while the sample to be plated was the cathode. Approximate distance between the anode and the cathode was 1.5"-2". The platings produced had a smooth interface (fig. III.6) and the average thickness of the platings was 15μm. Several microcracks (indicated by arrows) were present in the plating to relieve the stress build up during the plating process.

III.c Sectioning:

In order to minimize coating deformation, sectioning was performed with a low speed saw and diamond blade. Blade speed was held at approximately 120 rpm for a 4" wheel, and the vertical load on the sample was kept at approximately 260 gram. Cutting oil was used as the lubricant. The direction of cutting, or the tangential direction of blade rotation, was always kept into the coating surface.

III.d Heat-Treatment:

Isothermal heat treatments at 600^0C were conducted on the sectioned samples for 9 hrs, 22 hrs, 168 hrs, 500 hrs and 1000 hrs. All the samples were encapsulated under vacuum in quartz tubing before the heat treatments to limit oxidation. Isothermal heat treatments at 1000^0C were also conducted on a number of samples for 1.5, 2.5 and 4 hours. A constant flow of nitrogen gas was maintained during the heat treatment to prevent any oxidation.

III.e Oxidation Testing:

For oxidation testing, the samples were placed in a Lindburg tube furnace which was open at both ends. The test temperature was 600^0C and the exposure time were 100 hrs, 250 hrs and 500 hrs.

III.f Sulphidation Testing:

A schematic of the apparatus used for sulphidation testing is shown in figure III.7. The sulphur dioxide flow rate was kept constant at approximately 15mL/min. Nitrogen was used to purge the system before and after the samples were removed. The purpose of the test was to see if the microcracks in the plated chromium provide a diffusion path for sulphur. The temperature of the testing was 600^0C and the exposure times were 100 hrs and 250 hrs.

III.g Metallographic preparation:

For coated samples, Buehler cold-setting epoxide was used as mounting material. This was done to avoid any coating degradation which may occur when using hot press mounting techniques. In order to prevent any "rounding" of the plated edges, a support bar was placed close to the plated side(fig. III.8). Stabilizers and an indicator were included in each mount.

Hand grinding was done on rotating wheels on 120, 240, 320, 400 and 600 silican carbide grit papers. Samples were held against the wheel in a stationary position oriented either parallel or perpendicular to the wheel. The samples were rotated ninety degree after each grinding paper so that grinding was performed perpendicular to the direction

of the previous step. Samples were inspected after each grinding step under the light optical microscope to ensure that all scratches were uniform in direction. After grinding on the 600 grit paper, the mount was immediately wiped and flushed with alchohol. The mount was then blown dry and inspected in the light optical microscope. Polishing was performed by hand with steps including 6 micron diamond paste for approximately 1 minute, 0.5 micron alumina slurry for approximately 90 seconds and colloidal silica for 60 seconds. 4% picral was used to etch the samples after the polishing was complete.

III.h Sample Analysis Techniques:

Microstructural observation and photomicrography was conducted with the use of a Reichert-Jung MeF3 metallograph. Additional characterization procedures included the use of an ETEC Autoscan scanning electron microscope (SEM) with a KEVEX energy-dispersive x-ray spectrometer (EDS) and a JEOL 733 superprobe for X-ray wavelength dispersive spectrometry (WDS) elemental dot mapping. Quantitative analysis were also done for Fe, Cr and carbon to determine the composition profiles of these elements. The analysis were done at 15 Kev and a conventional $\phi(\rho Z)$ correction technique was used. An iron carbide (Fe_3C) standard was used to peak carbon in the microprobe analysis. Samples recieved a thin amorphous carbon surface coating before the electron microscope analysis to facilitate sample charge dissipation under the electron beam. For carbon analysis, the samples were coated with silver paint to facilitate sample charge dissipation. Semi-automated image analysis techniques were employed to obtain quantitative microstructural coating information. Measurements were made for the decarburized layer thickness

and the chromium layer thickness. For this purpose, a Donsanto Micro-plan II digitizing pad was used in conjuction with a Nikon Optiphot and an IBM personal computer.

IV. RESULTS AND DISCUSSION

IV.a Diffusion Studies At 600^{0}C

IV.a.1 Diffusion studies in ferrite

The microstructures of the columnar samples after the isothermal heat treatment at 600^{0}C for 22 hours are shown in figs. IV.1a and IV.1b. Fig. IV.1a shows the outer Cr layer, the layer of decarburized columnar grains below it and the substrate. Fig. IV.1b shows the needle like precipitates in the columnar sample after the heat-treatment. Some grain boundary carbides (marked g) are also visible. Fig IV.2a and IV.2b show the microstructure of the equiaxed samples after 22 hours of heat-treatment at 600^{0}C. There was no significant change in the needle like precipitate morphology or in the grain boundary carbides after the heat-treatment in the columnar or equiaxed samples. The precipitate distribution was uniform in both the columnar and equiaxed structures. No needle like precipitates were found 25-30μm below the Cr layer both before or after the heat-treatment. Figure IV.3 shows the Cr layer and the underlying decarburized layer at 1500X for the 22 hour sample. The Cr layer has microcracks (marked c) and a macrocrack (marked m). The macrocrack in the Cr layer forms due to low H_2SO_4/Cr_2O_3 (sulphate ratio) in the bath [31]. The sulphate ions in the plating bath aid in microcrack formation in the Cr layer. Thus, when the concentration of H_2SO_4 decreases in the plating bath, less microcracks form but macrocrack formation takes place. The mechanism by which the sulphate ions affect the microcrack and macrocrack formation is not well understood [31].

Figs. IV.4 and IV.5 are 1000X pictures of the chromium

layer and the underlying decarburized layer for the 168 hour heat-treated samples at the same temperature of 600^{0}C. The pictures show an interesting feature, the presence of a reaction layer below the Cr layer. The thickness of the reaction layer was 1.9μm ($\pm$0.22μm) in both the columnar and equiaxed samples. Fig. IV.6 shows the reaction layer at higher magnification. Fig IV.7 shows the reaction layer below the Cr layer after 500 hours of heat-treatment. The width of the reaction layer increased. On measurements it was found to be 3.3μm ($\pm$0.40μm). On close examination of the reaction layer (figs. IV.6 and IV.7), two layers can be seen in the reaction layer (arrows marked i indicate the interface between the two layers). Some surface relief (marked s in fig. IV.6) was present below reaction layer.

Figure IV.8a is a light optical picture (taken by Nomarski Interference Contrast technique) showing the presence of two layers in the reaction layer. The sample was heat-treated at 600^{0}C for 500 hours. Fig. IV.8b is a backscattered image showing the upper layer in the reaction layer (marked u) to be darker and of a lower atomic number than the Cr layer (marked Cr) and the Fe layer (marked Fe). A quantitative analysis of the elements Fe, Cr and carbon was done using electron probe microanalyser. Figure IV.9 shows the composition profiles of Fe, Cr and C from Cr layer into the decarburized layer (from point marked b in the Cr layer to a in the decarburized layer in figure IV.8b). The concentration profiles (fig. IV.9) indicate that there was nearly 100 wt% Cr in the chromium layer with extremely low amounts of Fe. Moving from Cr layer into the upper layer in the reaction layer (region marked u in fig. IV.9), there is a carbon peak containing nearly 5 wt% carbon. The chromium concentration drops and the Fe concentration increases in this layer. In the lower layer

of reaction layer (region marked l in fig. IV.9), there is a sharp drop in carbon concentration. The chromium concentration decreases further and the Fe concentration increases in this layer. Below the reaction layer (interface marked c with an arrow), there is a smoothly decreasing concentration profile of Cr and increasing concentration profile of Fe. As expected, the carbon level is extremely low in the decarburized layer.

WDS maps were also obtained to get a qualitative distribution of the elements—Fe, Cr, nitrogen and carbon in the chromium layer, reaction layer and the decarburized layer below the reaction layer. No nitrogen was detected. The maps (fig. IV.10) also indicate the presence of carbon in the reaction layer and in some cracks in the Cr layer. From the carbon map (fig. IV.10b), it can be seen that the upper layer in the reaction layer (marked u) is brighter than the lower layer (marked l) and hence is richer in carbon. The quantitative analysis of carbon in the two layers also indicated higher carbon in the upper layer. The interaction volume for X-ray generation is high for carbon (a calculation of the Kanaya-Okayama range [32] for carbon in Fe gives the value of $R_{ko} = 1.5\mu m$). It is possible that the carbon signals in the lower layer of the reaction layer (region marked l in fig. IV.10b) have a substantial contribution from the carbon signals in the upper layer (region marked u in fig. IV.10b). The wt% carbon in the reaction layer is above the solubility limit of carbon (a maximum of 0.1 wt% at 600^0C) in Fe-Cr alloys. Hence the carbon should be in form of carbides in the reaction layer.

The backscattered picture of the reaction layer (fig. IV.8b) shows the atomic number contrast and an element with a lower atomic number shows darker in a backscattered image. From fig. IV.8b it can be seen that the upper layer

in the reaction layer (marked u) is darker than the Cr layer (marked Cr) and the decarburized layer (marked Fe). Since a carbide has an atomic number lower than Fe or Cr (due to presence of low atomic number element carbon), the upper layer in the reaction layer should be a carbide rich layer. The lower layer in the reaction layer does not indicate much contrast with Fe. There can be two explanations for the formation of this layer. Based on the backscattered picture, this layer has almost the same contrast and atomic number as ferrite. Therefore this layer can be an iron rich layer with chromium and carbon in solid solution form. The reason for the interface formation with the decarburized layer is not clear. One of the possibilities is the initial nucleation of carbide which then grows in towards the Cr layer and subsequently forms the upper carbide layer [33]. Another explanation for the formation of this lower layer can be given based on quantitative analysis. The quantitative analysis show that the lower layer contains more than 0.1 wt% carbon. Hence carbon may be in the form of carbides in this layer. The backscattered picture does not show an atomic number difference with Fe in this layer and quantitative analysis indicate it to be an Fe rich layer. It is thus possible that this layer contains fine carbide precipitates in a ferrite matrix.

The formation of carbide layers has been observed during chromizing of various Fe-C alloys [25]. Carbide formation in the ternary Fe-Cr-C system has been studied using powder metallurgy methods [12,20]. In the present work, a diffusion couple technique was used to study the carbide formation in the Fe-Cr-C system at 600^{0}C. The diffusion couple consisted of an electrodeposited Cr layer on the top of a decarburized Fe-0.2%C substrate (fig.

III.4). Isothermal heat-treatments at 600^{0}C were performed on the diffusion couple for times ranging upto 1000 hours. The 'composition of the carbide formed using the above mentioned diffusion couple technique was analysed with the help of EPMA (region marked u in fig. IV.9). The carbide composition obtained corresponds very well to the $M_{23}C_6$ carbide composition found in the ternary Fe-Cr-C phase diagrams using powder metallurgy techniques [12,20].

The formation of a carbide layer in these diffusion experiments indicates that there is a source of carbon. The starting diffusion couple consisted of pure chromium in contact with almost pure Fe (decarburized ferritic layer). During the heat-treatment carbon also diffused in towards the Cr layer and formed a carbide layer in the reaction layer. There are two sources of carbon, the iron carbide particles in the pearlite and the dissolved carbon in the decarburized layer (a maximum of 0.005 wt% which is the solubility limit of carbon in ferrite at room temperature). At a temperature of 600^{0}C, the solubility of carbon in ferrite increases to 0.01 wt%. Hence, carbon can come from the solutionization of iron carbide particles in pearlite. Thus, the source of carbon for the carbide formation in the reaction layer is the dissolved carbon in ferrite. Since carbon is an extremely mobile element and chromium has a high affinity for carbon, carbon in solution diffused during heat-treatment to form carbides in reaction layer.

IV.a.2 Ternary Diffusion Paths

Figure IV.11b shows the possible diffusion path from the decarburized layer to the chromium layer (from point a to point e in figure IV.11a). Points a to b are in the decarburized layer, point b to point c is in the lower layer of reaction layer indicating the presence of carbide

precipitates in the Fe rich ferrite matrix. Point c to point d is in the upper layer of the reaction layer and indicates the possibility of a chromium rich $M_{23}C_6$ carbide layer. Point d to point e is in the Cr layer. Figure IV.12b shows another diffusion path in which the lower layer in the reaction layer (points b to c in fig. 12a) is considered to be a ferritic layer with dissolved carbon and chromium. Point c to point d indicate the possibility of a chromium rich $M_{23}C_6$ carbide layer.

IV.a.3 Reaction Layer Thickness Variation Estimations

The width of the reaction layer in the 1000 hour sample was 4.5μm($\pm$0.45μm). The thickness of the reaction layer varied with time in a parabolic manner (Fig. IV.13). In general, the simplified diffusion equation can be written as $x^2 = 4Dt$ [34], here x is the diffusion distance in cm, D is the diffusion coefficient in cm^2/s and t stands for time in seconds. Thus the various equations for the variation of Reaction Layer Thickness (RLT) and for Fe and Cr diffusion with time can be written as:

$$(RLT)^2 = 4*1.35exp(-14)*t \text{ ---------- (i);}$$

$$x^2 = 4*9.67exp(-15)*t \text{ ---------- (ii);}$$

$$x^2 = 4*1.52exp(-14)*t \text{ ---------- (iii);}$$

From equations (ii) and (iii), the values of diffusion coefficients are; D(Cr in α-Fe) = $9.67*10^{-15}$ cm^2/s and D(Fe in Cr) = $1.52*10^{-14}$ cm^2/s [35] respectively. Thus the value of the diffusion coefficient for RLT, D = $1.35*10^{-14}$ cm^2/s, closely matches the values for the diffusion of Cr in α-Fe and of Fe in Cr at 600^0C. Table 4 shows the calculated values of RLT for longer time periods assuming that the above relation(i) holds true.

IV.a.4 Coating Thickness Calculations

An estimation of the consumption of Cr layer with time can be done by assuming that the carbide layer in the reaction layer is consuming the chromium layer. Thus the increase in thickness of the carbide layer gives an approximate idea of the amount of Cr layer consumed. From fig. IV.9 (region marked u in fig. IV.9), the width of the carbide layer in the reaction layer was measured to be nearly 1μm. The carbide layer thickness should follow a parabolic relation;

$$(CLT)^2 = 1*10^{-3}*t \text{ ---------- (iv)}$$

In equation (iv) CLT stands for carbide layer thickness in microns and t stands for time in hours. If the approximation of Cr layer consumed being equal to the carbide layer thickness (region marked u in fig. IV.8b) is taken, it will give an idea of the consumption of chromium layer with time. Fig. IV.14 shows the plot of Cr layer consumed vs time (calculated using equation (iv)). It can be seen that after 100000 hours (approximately 11 years) the thickness of the Cr layer consumed would be about 10μm and after 200000 hours (approximately 23 years), the thickness of the Cr layer consumed would be only 14μm. The significance of the above numbers lies in the fact that they indicate that the minimum thickness of the outer Cr layer in the chromized coatings (marked Cr in fig. I.1) needed to survive for 200000 hours (at 600^{0}C) would be in excess of 14μm. The thickness of the this Cr layer needed to survive at lower temperatures would be less.

IV.a.5 Decarburized layer thickness variation studies

A study of the variation in the decarburized layer

thickness with time at 600^{0}C was also done. The heat-treatment temperature (600^{0}C) is below the eutectoid temperature (723^{0}C). Above the eutectoid temperature, ferrite and pearlite would transform to austenite which has high solubility for carbon. At 600^{0}C, pearlite would not solutionize to austenite. It was expected that the decarburized layer thickness will remain constant with time. The results of the experiments are shown in fig. IV.15. Within the limits of error, the depth of the decarburized layer remained almost constant with time.

Summary

Diffusion studies at 600^{0}C (in a diffusion couple of pure Cr and decarburized Fe above a substrate containing 0.2% C), led to the formation of a reaction layer below the Cr layer. The reaction layer consists of two layers. The use of various electron microscopy techniques indicates the possibility of one of the layers in the reaction layer to be a carbide layer containing nearly 5 wt% carbon. The formation of this carbide layer takes place during the isothermal heat-treatment (at 600^0) due to the diffusion of carbon from the decarburized ferritic layer towards the Cr layer. The composition of the carbide layer indicates the possibility of an $M_{23}C_6$ carbide (from the ternary phase diagram). The other layer in the reaction layer can be a solid solution of Fe, Cr and carbon or a ferritic layer containing fine carbide precipitates. The thickness of the reaction layer increased with time in a parabolic manner. An estimation of the consumption of Cr layer from the carbide layer thickness indicated that the minimum thickness of the outer Cr layer in the chromized coatings (marked Cr in fig. I.1) needed to survive for 200000 hours would be in excess of 14μm.

IV.b Diffusion Studies at 1000^{0}C

IV.b.1 Diffusion studies in austenite

The austenite (γ) phase usually aids in large carbon movement. The structure of the γ phase is close packed FCC, while that of α is BCC, hence the magnitude of the diffusion coefficient of carbon is greater in α. But the maximum solubility of carbon in γ-iron(2.0 wt%) is much greater than in α-iron(0.02 wt%) due to much larger octahedral holes in austenite [36]. As a result of that, there is a large uptake of carbon in the austenite phase. A diffusion study was done at 1000^{0}C for 4 hours to observe the carbon redistribution in the sample. The starting microstructure before the heat-treatment at 1000^{0}C was as shown in fig. IV.16, i.e., pearlite plus ferrite below the decarburized ferritic layer. At the heat treatment temperature (1000^{0}C), the microstructure is wholly austenitic. Figs. IV.17a and IV.17b show the resulting microstructure after the heat-treatment. It can be seen that carbon has diffused throughout the decarburized layer in just 4 hours forming ferrite and pearlite. At the heat-treatment temperature, there was a large concentration gradient of carbon from the substrate (0.2% carbon) to the decarburized layer (maximum 0.005% carbon). Therefore, at the heat-treatment temperature when the microstructure is all austenitic, carbon diffused into the decarburized layer with time. As a result of carbon moving into the decarburized layer, ferrite and pearlite form below the eutectoid temperature during slow cooling.

IV.b.2 Chromizing simulation studies

To gain a further understanding of the microstructure of chromized coatings, a chromizing simulation procedure

using electrodeposited chromium instead of the conventional pack method [37-39] was tested. In the simulation procedure, the sample was heat-treated at 1000^{0}C for 4 hours in a nitrogen atmosphere. The microstructure of the sample before the heat-treatment consisted of a Cr layer on the top of the decarburized columnar layer above a substrate containing ferrite and pearlite (fig. III.4). Two types of microstructures were obtained in the same specimen after the heat-treatment due to the differences in the decarburized layer thickness at the corners and away from the corners. Fig.IV.18 shows the greater thickness of the decarburized layer at the corners before electroplating or heat-treatment. Figs. IV.19a and IV.19b show a schematic representation of the macrostructure near the corners before and after the chromizing simulation procedure. The resultant chromized microstructure obtained near the corners after the heat-treatment is shown in figs. IV.20a and IV.20b. This is similar to the typical chromized microstructure shown in figs. IV.21a and IV.21b [3]. Below the outer Cr layer it had columnar grain carbides (marked g), intragrain carbides (marked c) and random large voids (marked v) (fig. IV.20a). In fig. 20b the voids can be seen to be surrounded by a carbide (arrows marked k). Away from the corners of the sample, the structure gradually became pearlitic in nature (see region marked pearlite in fig. IV.19b). Fig. IV.22 shows the microstructure changing to pearlitic (corresponding to a small region between the regions marked chromized and pearlite in fig. IV.19b). In fig. IV.22 the carbides (marked c) and the pearlite (marked p) can be seen. The pearlite near the right end of the figure (marked p) was very fine and could not be resolved in a light optical microscope at 800X. Figs. IV.23a and IV.23b show the microstructure away from the corners at two different magnifications (corresponding to the region

marked pearlite in fig. IV.19b). It seems to be completely pearlitic in nature. The structure below the pearlitic or chromized layer is severely decarburized and grains were equiaxed (fig. IV.24) as opposed to columnar before the heat-treatment (fig. III.4).

An explanation for the change in the microstructure from the corners to the center can be given as follows. The microstructures formed above are composition dependent and there is a difference in composition at the corners and away from the corners due to the difference in decarburized layer thickness. During the heat-treatment, when the sample is in the high temperature γ phase region, the diffusion of carbon is greatly enhanced in the presence of the chromium layer. Hence, carbon moves through the decarburized layer into the chromium layer. The effect of carbon on the Fe-Cr system is to widen the γ loop [40]. Conversely, the effect of chromium on the Fe-C system is to raise the eutectoid reaction temperature and to lower the eutectoid carbon content (fig. IV.25) [41]. For example, it can be seen from figure IV.26 that the addition of just 15 wt% Cr can give a fully pearlitic structure on slow cooling even with 0.35 wt% C. As a result of the upward movement of C towards chromium layer, and the diffusion of Cr into the decarburized layer, a composition giving rise to the eutectoid reaction [42] $\gamma \rightarrow \alpha + Fe_3C$ is easily reached. This can cause the formation of a pearlitic structure as seen in the figures IV.23a and IV.23b. Near the corners, the thickness of the decarburized layer was greater (fig. IV.18), hence in a given time, the carbon content was less at the corners. Thus the carbon concentration was not enough to give rise to the eutectoid reaction. As a consequence, at the corners a microstructure similar to the chromized coating microstructure was seen instead of

pearlite formation. Thus the amount of carbon diffusion can be restricted by decreasing the time of heat-treatment. This would prevent the eutectoid composition to be reached and hence give rise to a chromized coating microstructure.

To prove the above point, a few heat-treatments of shorter durations (one and half hours compared to 4 hours) were performed. A microstructure similar to the chromized coating microstructure was induced everywhere below the chromium layer. Figures IV.27a and IV.27b show the micrographs of the resulting microstructure. The samples were furnace cooled after the heat-treatments. The microstructure is exactly similar to the usual chromized coating microstructure (figs. IV.21a and IV.21b) containing the voids and the columnar grain boundary carbides (indicated by arrows in fig. IV.27b). This indicated that the carbide formation in the chromized coatings is dependent on the thermal cycle (heat-treatment time and heating and cooling rates) at temperatures above the eutectoid temperature. Longer heat-treatment times at temperatures above the eutectoid temperature during the heating and cooling process lead to more carbon diffusion in the coating and hence more carbides (or pearlite) form. Thus the extent of carbide formation can be decreased by decreasing the heat-treatment time above the eutectoid temperature.

The severe decarburization in the substrate below the chromized layer (region marked decarb in fig. IV.24) suggests that both the austenitic phase and the Cr layer have aided in large uptake of carbon. The movement of carbon was to such a great extent that it diffused through the decarburized layer and again formed a decarburized layer below the coating. An explanation for the formation of the decarburized layer below the coating (region marked

decarb in fig. IV.24) can be given as follows. The starting microstructure of the sample before the heat-treatment had a decarburized layer (500 microns thick) below the Cr layer (fig. III.4). During the heat-treatment at 1000^0C, carbon from the substrate moved towards the Cr layer through the decarburized layer. If the Cr layer was not present, then the microstructure after the heat-treatment would be the same as fig. IV.17, i.e., pearlite and ferrite throughout the sample. The presence of the Cr layer causes a large uptake of carbon in the form of carbides in the chromized layer. As a consequence, when a sample containing a Cr layer above the decarburized layer (fig. III.4) is heat-treated at 1000^0C, a decarburized layer (nearly 450 microns thick) again forms below the chromized layer after the heat-treatment (region marked decarb in fig. IV.24). This is not very surprising considering the fact that the carbon content in the chromized coatings has been found to be as much as eight times that of the substrate [43]. The equiaxed grain shape in the decarburized layer after the heat-treatment (fig. IV.24) as opposed to columnar before the heat-treatment (fig. III.4) indicates that the formation of equiaxed grains takes place during the heat-treatment so that the decarburized layer thickness is unrelated before and after the heat-treatment.

In order to study the effect of cooling rates on the microstructure, some samples were quenched in oil instead of being furnace cooled after being heat-treated at 1000^0C for 4 hours. The microstructure obtained was mostly bainitic (IV.28a and IV.28b). A carbide layer (shown by arrow) was present below the Cr layer. No columnar grain carbide structure was formed nor did any decarburization take place in the time durations ranging from one and a half to four hours. This shows that during the actual

chromizing process, the formation of columnar grain boundary and intragrain carbides takes place during slow furnace cooling (from 1000^0C to room temperature in approximately 5 hours or 200^0C/hr). The formation of columnar grains takes place in the two phase ferrite and austenite region [29]. In the chromizing process, the two phase ferrite and austenite region occurs due to the nucleation of ferrite on austenite grain boundaries during slow cooling. Formation of columnar grains takes place in this two phase region and the subsequent precipitation of carbides on the boundaries of these columnar grains possibly forms the chromized coating microstructure (figs. IV.21a and IV.21b). The absence of the decarburized layer on quenching indicates that a good amount of carbon movement takes place during slow cooling.

The voids usually present in the microstructure were absent in the quenched samples. This indicates that the void formation occurs by some mechanism other than diffusive mass transfer imbalance or the Kirkendall Effect [44]. If the Kirkendall Effect was responsible for their formation, then they should have formed at the heat-treatment temperature and remained on quenching. No halide activators were used in the expriments. Thus the void formation due to halide activators [5] is also not possible.

Since the voids are surrounded by carbides (fig. 20b), the vacancy-interstitial interaction [27] is a possibility for their formation. The vacancy-interstitial interaction as explained by Damask [45] based on Lazarus's [46] and Mott's [47] theories can be stated as follows. Whenever there is a positive binding energy between vacancies and interstitials, some of the vacancies will be bound to the interstitials [45]. Two important energy terms are expected

to give rise to the binding energy of a vacancy to an interstitial, namely, the change in the strain energy around the vacancy and the electrostatic interaction between the vacancy and the interstitial. Since the interstitial (for example carbon) differs in size from the host atom (for example Fe), the strain surrounding the interstitial may be relieved by placing a defect adjacent to the interstitial [45]. Since the distortion around an interstitial is quite large, the strain relief obtained upon trapping an interstitial can be considerable. The approach to the electrostatic bonding of a vacancy to an interstitial was given by Lazarus [46] based on Mott's treatment of the screening of an interstitial atom by the Fermi electrons. According to Mott [47], the excess ionic charge, Z, of the interstitial atom will be screened on the basis of the linearized Thomas-Fermi equation by an interaction potential of the form: $\phi(r) = Ze/r \exp(-qr)$, where r is the distance from the center of the interstitial, e the electronic charge, and q is a constant. The neighboring solvent atoms around an interstitial will, therefore, be repelled by a Coulomb force in addition to the usual closed-shell repulsive forces. Consequently, the binding energy of these atoms is decreased and therefore it takes less energy to remove one of these neighboring atoms from the lattice. The decrease in the binding energy of these atoms is equal to the change in the energy required to form a vacancy at a site adjacent to the interstitial.

Fergusan and coworkers [48] report the diffusion of tightly bound vacancy-carbon atom pairs diffusing as entities in their studies of Pt-C alloys. They also report the occurance of strong binding between vacancies and interstitial carbon atoms in Fe and other metals. It gives the idea that vacancy-interstitial interaction may be a

possible mechanism for vacancy (surrounded by carbide) formation in chromized coatings.

Summary

Diffusion studies at 1000^{0}C gave important information about the chromized microstructure formatiom mechanism. The chromized coating microstructure formation is dependent on time and heating and cooling rates in the heat-treatment procedure. The amount of carbon diffusion into the coating is controlled by the thermal cycle (heat-treatment time and heating and cooling rates) at temperatures above the eutectoid temperature in ternary Fe, Cr, C system. Longer durations of heat-treatment lead to large carbide formation (or a pearlitic microstructure) in the coating. Thus the amount of carbide formation and hence the coating microstructure can be altered by controlling the thermal cycle above the eutectoid temperature. The typical chromized microstructure (carbides, voids) is predominantly caused by slow furnace cooling. Quenching the samples after the heat-treatment does not give the typical chromized microstructure (carbides, voids). This indicates that the columnar grain carbide formation and the void formation takes place during slow cooling in the chromizing process. Since the voids are surrounded by carbide, vacancy-interstitial interaction is a possibility for their formation.

IV.c Oxidation Testing

Since boiler tubes usually operate in oxidizing environments, tests were done to see the behavior of an as-plated chromium coating in oxidizing environment. The study of the behavior of microcracks in the plating under oxidizing conditions was especially important. These

microcracks are believed to be localized regions of different oxygen concentration, probably chromium oxides [49]. Figure IV.29 shows the microstructure of as plated chromium above the substrate. Microcracks (arrows) can be seen in the as-plated condition. Fig. IV.30 shows the microstructure of the Cr layer after 100 hrs of heat-treatment at 600^{0}C. Arrows indicate the oxidation attack at the microcracks (marked a) and the joining of the microcracks to form larger microcracks (marked b). The size and area fraction of the microcracks in the chromium layer also seems to increase after the heat-treatment. Figs. IV.31 and IV.32 show the microstructure of the chromium layer after 250 hrs and 500 hrs of heat-treatment respectively. Oxidation attack at the microcracks (marked a in the figures) and the joining of the microcracks (marked b in the figures) can also be seen in these pictures. In fig. IV.33 the area fraction of the microcracks in the chromium layer vs the heat-treatment time is plotted. In fig. IV.33b the data shows a logarithmic relationship. It can be seen that the area fraction of the microcracks increases sharply during first 100 hours of heat-treatment and then increases with time at a very slow rate. Thus, the kinetics of the increase in area-fraction of microcracks follows a logarithmic relationship. Table 5 shows the variation of the average length and width of the microcracks with time. It follows the same trend as that of the area fraction.

An increase in the microcrack size and area fraction can be attributed to the oxygen entering the microcracks and forming an oxidation product. This oxidation product being of larger volume than the microcracks leads to an increase in crack size. The thermal stresses generated (due to the differential thermal expansion between Fe and Cr)

may generate tensile stresses in the Cr layer that can lead to the propagation of the microcracks. An increase in the area fraction of the microcracks is mainly due to the increase in crack size. It is quite possible that some cracks that could not be seen before the heat-treatment opened up during the heat-treatment thus contributing to an increase in the area fraction of the microcracks. The logarithmic kinetics of oxidation attack at the microcracks suggests that the attack reaches a constant level after some time. It seems likely that chromium oxide forms in the microcracks due to the oxygen entering the microcracks and the subsequent attack stops. Thus, these microcracks can be detrimental to the coating properties to a limited extent. In order to get the beneficial corrosion resistant properties of the Cr layer, a control over these microcracks is needed. If crack free electroplated chromium could be produced, it might prove very beneficial for corrosion resistance.

IV.d Sulphidation Testing:

The purpose of the sulphidation testing of the Cr layer was to see if the microcracks in the Cr layer would provide a diffusion path to the base metal for the gas in a SO_2 gas environment. Fig. IV.34 shows the phase stability diagram of the Cr-S-O system at 627^0C [50]. It can be seen from fig. IV.34 that the Cr_2O_3 is predominantly the stable phase in this system. A calculation of partial pressures of oxygen (p_{O_2} = 8.2×10^{-13} atm) and gaseous sulphur (p_{S_2} = 1.6×10^{-12} atm) using the SOLGASMIX program [51,52] indicate that Cr_2O_3 formation will take place in a pure SO_2 environment (point marked x in fig. IV.34). Fig. IV.35 shows the microstructure of the chromium layer after 100 hours of heat-treatment at 600^0C in sulphur dioxide

environment. Arrows (marked a) indicate the attack on the microcracks by the gas. Other features to be seen are the lateral growth of the cracks (marked d in the figure) and the sulphidation product at the top of the coating (marked c in the figure). Microcrack size and area fraction has also increased compared to the as-plated specimen (fig. IV.33 and table 5). Within the limits of error, the kinetics of sulphidation attack at the microcracks followed a logarithmic relationship. The rate of attack is greater in the sulphidation environment (compared to the oxidation environment) as seen in the logarithmic expressions in fig. IV.33b. Since chromium oxide is the stable phase in a sulphur dioxide environment, it is possible that the chromium oxide fills the microcracks and limits further attack.

Fig. IV.36 shows the microstructure of the sample heat-treated for 250 hrs. Arrow (marked a in the figure) shows the sulphidation attack at the microcracks reaching the base metal (marked a in the figure). The sulphidation product at the top (marked c in the figure) and the lateral crack growth (marked d in the figure) can also be seen. Figure IV.37 shows the attack at the microcrack reaching the base metal (marked a in the figure) at higher magnification. An increase in the microcrack size and area fraction during sulphidation testing can be attributed to SO_2 or O_2 attacking the microcracks and forming a corrosion product. This corrosion product being of larger volume than the microcracks [10] can lead to an increase in the crack size. The thermal stresses generated (similar to the case of oxidation testing) can also lead to the propagation of cracks and the lateral or perpendicular growth of cracks (see fig. IV.33 and Table 5).

Summary

The microcracks in the as-plated chromium were attacked in oxidation and sulphidation environments. The size and area-fraction of microcracks in the Cr layer increased with time in oxidation and sulphidation tests. The increase in size and area fraction of microcracks can be attributed to the SO_2 or O_2 attacking the microcracks and forming a corrosion product. This corrosion product being of larger volume than the microcracks can lead to an increase in the size and area fraction of microcracks. The thermal stresses generated (due to differential thermal expansion between Fe and Cr) may generate tensile stresses in the Cr layer that can also lead to an increase in crack size. The kinetics of increase in the area fraction of microcracks followed a logarithmic relationship and the rate of attack was greater in the sulphidation environment. The logarithmic relationship indicates that the attack reaches a constant level after some time. It seems likely that the corrosion product (possibly chromium oxide) forms inside the microcracks and stops further attack.

V. CONCLUSIONS

The results of the above investigation lead to the following conclusions:

1) The grain shape i.e. columnar or equiaxed does not have any effect on the diffusion of carbon at 600^0C. There was no significant change in the needle like precipitate morphology or the grain boundary carbides in the columnar or equiaxed samples after the heat-treatment.

2) The austenite phase is responsible for the large movement of carbon during chromizing. This carbon poisoning leads to the formation of carbides and voids (on cooling) in the coating which are detrimental to the coating properties. The formation of a microstructure similar to the chromized coating microstructure at the high temperature indicates that chromized coatings can also be formed by the electrodeposition of chromium if the sample is properly heat-treated. The heat-treatment time and the heating and cooling rates above the eutectoid temperature are the essential steps that need to be controlled to get a typical chromized microstructure. Longer heat-treatment times can give rise to a completely pearlitic microstructure instead of chromized microstructure on slow cooling. Slow furnace cooling gives a chromized microstructure. The chromized microstructure was absent when the samples were quenched. The absence of a chromized coating microstructure on varying the cooling rate signifies the importance of cooling rate on the coating microstructure. It shows that the columnar grain carbide formation and the void formation are predominantly caused by slow furnace cooling.

3) The absence of voids in the quenched samples indicates that they form in slow cooled specimens due to the occurance of vacancy-interstitial interaction since the voids were surrounded by a carbide.

4) Diffusion studies in the ferritic microstructure at 600^0C led to the formation of a reaction layer below the chromium layer. Two layers were present in the reaction layer. The width of the reaction layer increased with time in a parabolic manner. Quantitative analysis and WDS mapping with the electron probe microanalyser indicated the presence of carbon in the reaction layer. Backscattered images indicated the possibility of one of the layers in the reaction layer to be a carbide layer. The other layer may be a solid solution of Fe, Cr and carbon or it may contain fine carbide precipitates in a ferrite matrix.

5) The microcracks in the electroplated chromium are prone to attack in the high temperature oxidation and sulphidation environments. An increase in the size and area fraction of microcracks in the Cr layer is observed during the high temperature heat-treatment. The kinetics of oxidation and sulphidation attack at the microcracks followed a logarithmic relationship which indicates reaching a constant level with increasing time. Thermodynamics predicts that Cr_2O_3 will fill the microcracks and therefore further attack will be arrested, as indicated by the corrosion kinetics. A further control over these microcracks is necessary to get longer life of the chromium layer in corrosive environments.

VI. REFERENCES

1. I.G. Wright, D.N. Williams and A.K. Mehta: Boiler Tube Failures in Fossil Plants(Proc. Conf.), EPRI, Polo Alto, California, 1987

2. Metals Handbook, American Society for Metals, 8th edn., 1961

3. B.J. Smith and A.R. Marder: Surface Modifications Technology 4, T.S. Sudershan, D.S. Bhat and M. Jeandin eds., The Minerals, Metals and Materials Society; Warrendale TMS, 1991, 471

4. R.A. Rapp, D. Wang and T. Weisert: in High Temperature Coatings, M. Khobaih and R.C. Krutentat eds., The Metallurgical Society, Warrendale

5. C. Cheng, G.H. Meier, R.A. Perkins and W.T. Bakker: Materials for Coal Gasification, W.T. Bakker ed., ASMI Metals Park, OH, 1988

6. A.J. Perry and E. Hovarth: J. Mater Sc., 13, 1978, 1304

7. K. Kuo: JISI, 171, 1953, 363

8. S.J.R. Saunders and J.R. Nicholls: Mater. Sci Eng A, vol. 5, 1989, 780

9. G.H. Meier, C. Chang, R.A. Perkins and W. Bakker: Surf Coat Technol, 39/90, 1989, 54

10. Personal Communication with Brian J. Smith, Energy Research Center, Lehigh University, Bethlehem, PA, June 1992

11. J. Chipman: Met. Trans., 3, 1972, 55

12. V. G. Rivlin: International Metals Review, 1984, 29, No. 4, 299

13. A.H. Sully and E.A. Brandes: 'Chromium', 2nd Edn., 77-82, 1967, London, Butterworths

14. J.C. Bailer (Ed.): Comprehensive Inorganic Chemistry,

vol. 3, 1973, Pergamon press, 624

15. F.A. Shunk: 'Constitution of Binary Alloys', Second Suppl., 1969, NY, Mcgraw Hill

16. M. Hanson and K. Anderko: 'Constitution of Binary Alloys', First Suppl., 1958, NY, Mcgraw Hill

17. B. Chicco and W.R. Thrope: Metall. Trans., 1982, 13A, 1293

18. E.K. Storms: 'The Refractory Carbides', 106, 1967, NY, London, Academic Press

19. K. Bungardt, E. Kunze and E. Horn: Arch Eisenhuttenwes, 1958, 29(3), 193

20. L.R. Woodyatt and G. Kruass: Metall. Trans., 1976, 7A, 983

21. R. Benz, J.F. Elliot and J. Chipman: Metall. Trans., 1974, vol. 5, 2225

22. R.L. Samuel and N.A. Lockington: Metal Treatment and Drop Forging, 1951, vol. 18, 352

23. N. V. Karyakina and G.N. Dubinin: Phys. Metals Metallography, 1960, vol. 9, 381

24. Y. Komen, B.Z. Weiss and S. Niedzwiedz: JISI, vol. 206, 488

25. L. Zancheva, M. Hillert, L. Staffarsson and S. Seetharaman: Metall. Trans., vol. 9A, July 1978, 911

26. W. Kaluba and A. Wachowaik: Arch. Eisenhuttenwes, 54, 1983, No. 4

27. I.A. Menzies and A. Mortimer: Corr. Sc., 1965, vol. 5, 539

28. A.R. Marder: Transactions of the Metallurgical Society of AIME, vol. 245, 1969, 1339

29. P.J. Adjema and D.J. Knight: Transactions of the ASM, vol. 56, 1963, 574

30. Metals Handbook: American Society for Metals, 9th edn., vol. 9

31. Personal communication with Dr. Alan Jones: Atotech USA

Inc., Somerset NJ, June 1993
32. J.I. Goldstein, D.E. Newbury, P. Echlin, D.C. Joy, C. Fiori and E. Lifshin: Scanning Electron Microscopy and X-ray Microanalysis, Plenum press, NY, 1984
33. Personal communication with Dr. J.I. Goldstein: Lehigh University, Bethlehem, PA, July 1993
34. P.G. Shewmon: Diffusion in Solids, J. Williams Book Company, OK, 1983
35. D.J. Fisher (Ed.): Defect and Diffusion Data Form, vol. 76, 1991, 189
36. Anil Kumar Sinha: Ferrous Physical Metallurgy, Butterworth Publishers, Stoneham, MA, 1989
37. P.C. Mukherjee: J. Electrochem. Soc. India, 30-3, 1981, 243
38. R. Drewett: Corrosion Science, 9, 1969, 823
39. K.K. Yee: International Metals Review, 1984, vol. 29, No. 4, 312
40. C.A.C. Sequira and C.M.G.S Nunes: Surf. Eng., 1987, vol. 3, no. 2, 159
41. E.C. Bain and H.W. Paxton: Alloying Elements in Steel, American Society for Metals, Metals Park, Ohio, 1961, 104
42. D.W. Rudorff: Metallurgia, 1945, 32, 59
43. R.L. Samuel and N.A. Lockington: Metal Treatment and Drop Forging, Oct. 1951, 442
44. Y.H. Son and J.E. Morral: Met Trans A, vol. 20, no. 11, Nov. 1989, 2299
45. A.C Damask and G.J. Weines: Point Defects in Metals, Gordon and Breach Science Publishers, NY, 1963
46. D. Lazarus: Physical Review, 93, 1964, 973
47. N.F. Mott: Proceedings Cambridge Philosophical Society, 32, 1936, 281
48. P. Ferguson, K.H. Westmacott, R.M. Fisher and U. Dahmen: Materials Science and Technology, January 1985, 1, 53

49. A.R. Jones: Plating and Surface Finishing, April 1989, 62

50. F.S. Chou, P.L. Danial, and R.F. Dudek: High Temperature Corrosion in Energy systems (Proc. Conf.), Michael F. Rothman, ed., AIME, NY, 1985, 327

51. G. Eriksson: Chemica Scripta, 8, 1975, 100.

52. R. Flynn, A.E. Morris and D. Carter: Using the UMR/SOLGASMIX software package, Proc. Computer Software Conference, Dept. of Metallurgical Engineering, University of Missouri-Rolla, Rolla, MO, 1987.

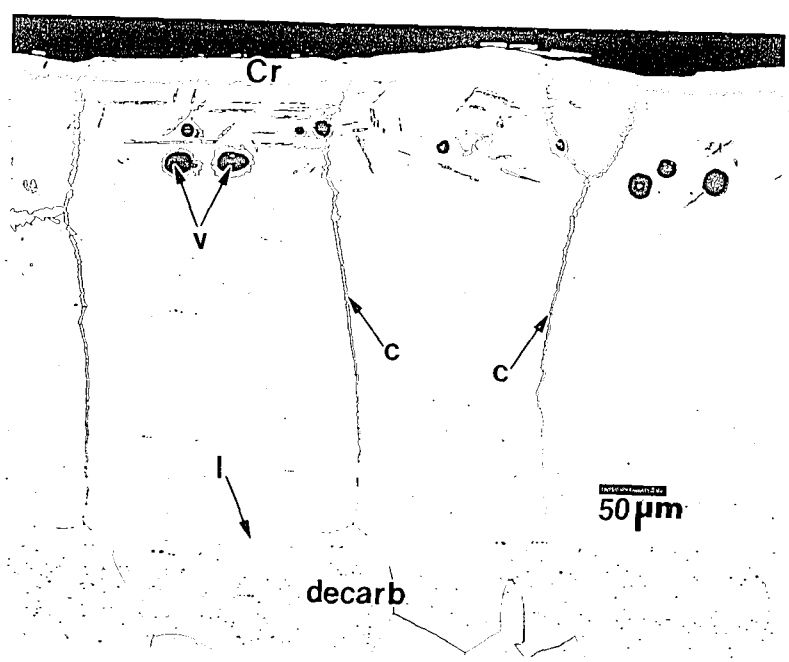

Fig. I.1 Typical microstructure of a chromized coating (figure courtesy Brian J. Smith[3]). (LOM 200X)

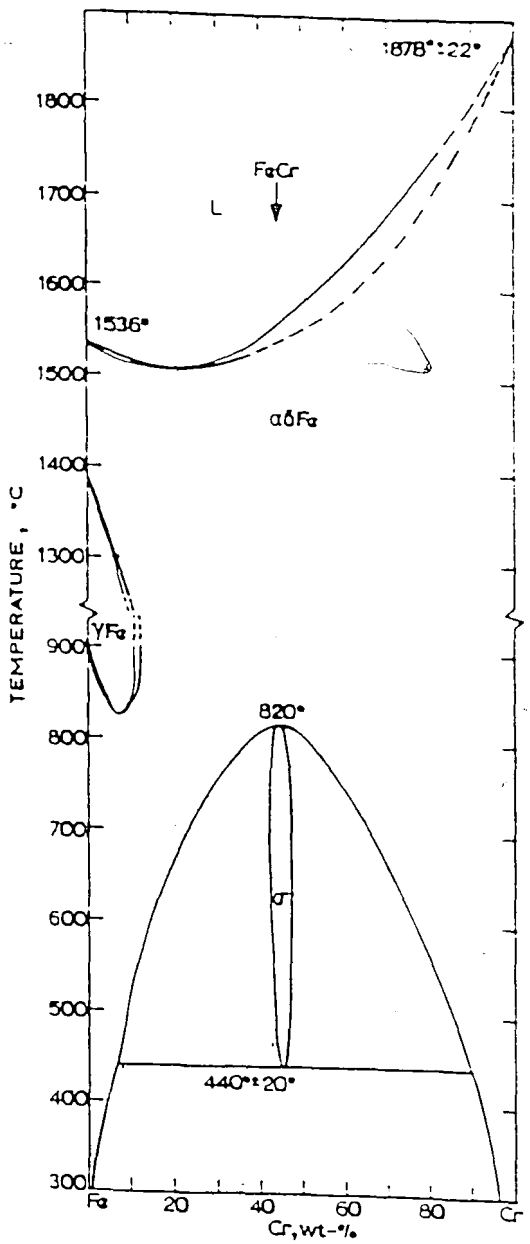

Fig. II.1 Fe-Cr phase diagram (reference 15).

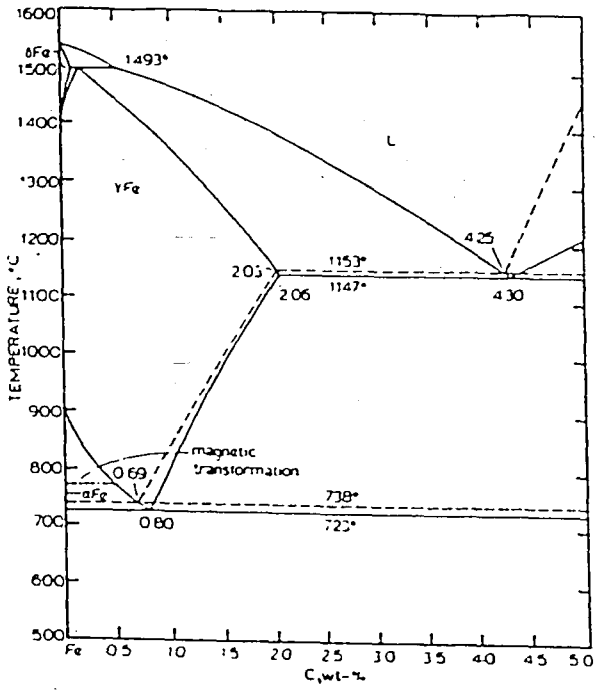

Fig. II.2 Fe-C binary system (reference 16).

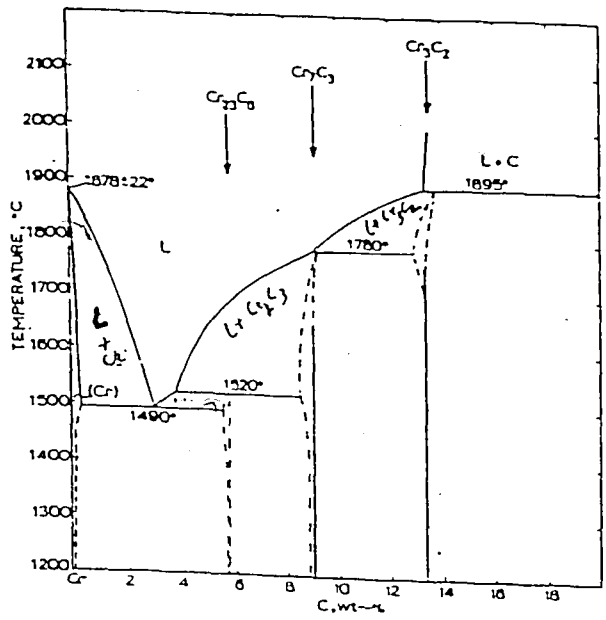

Fig. II.3 Cr-C binary system (reference 18).

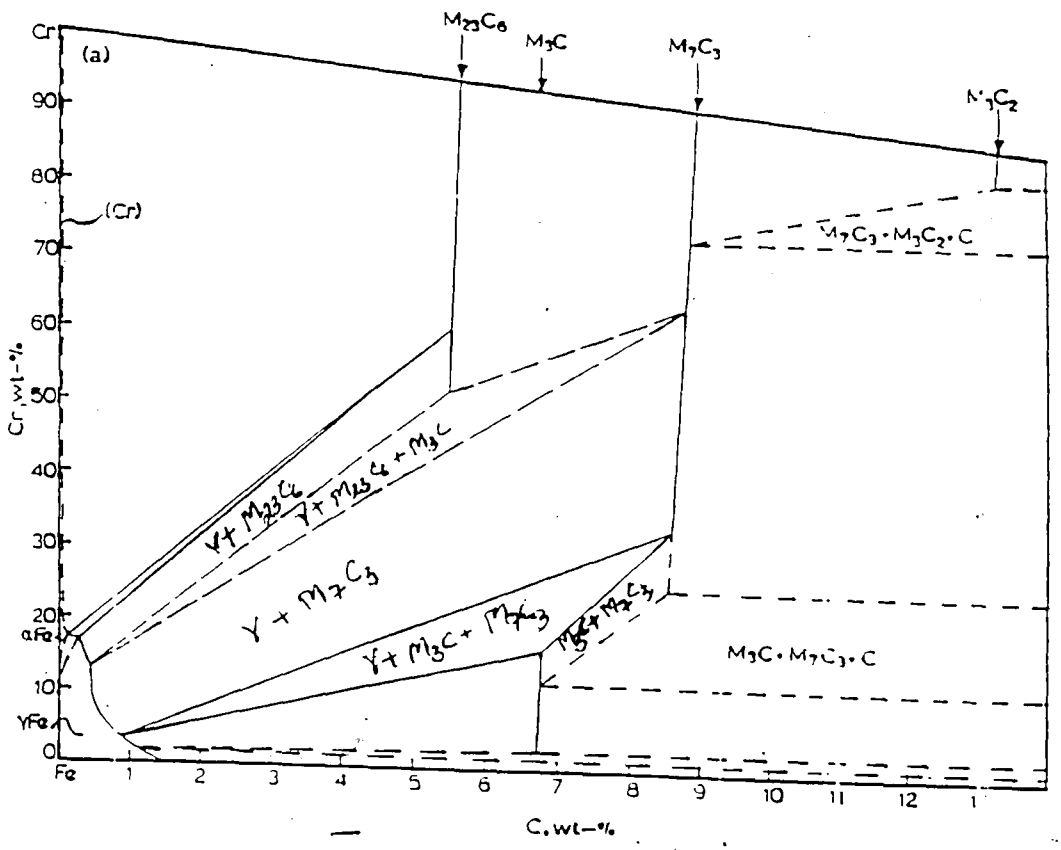

Fig. II.4 Phase relationships in the Fe-Cr-C system at 1000^0C (reference 19).

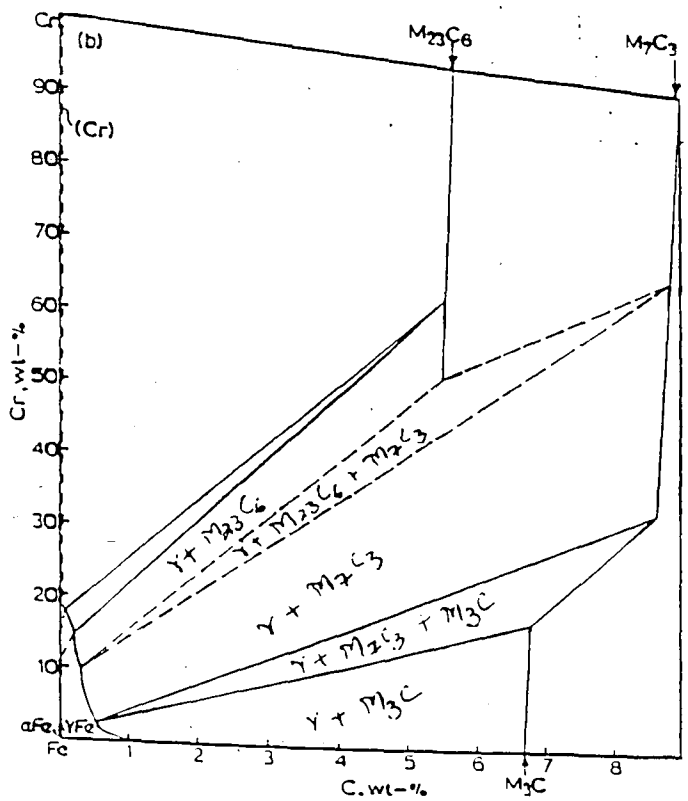

Fig. II.5 Isothermal section of the Fe-Cr-C system at 870^{0}C (reference 20).

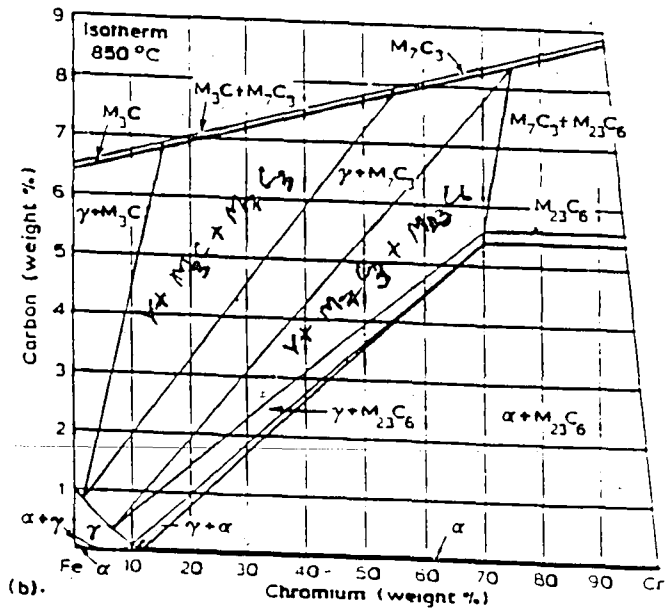

Fig. II.6 Isothermal section of the Fe-Cr-C system at 850^{0}C (reference 12).

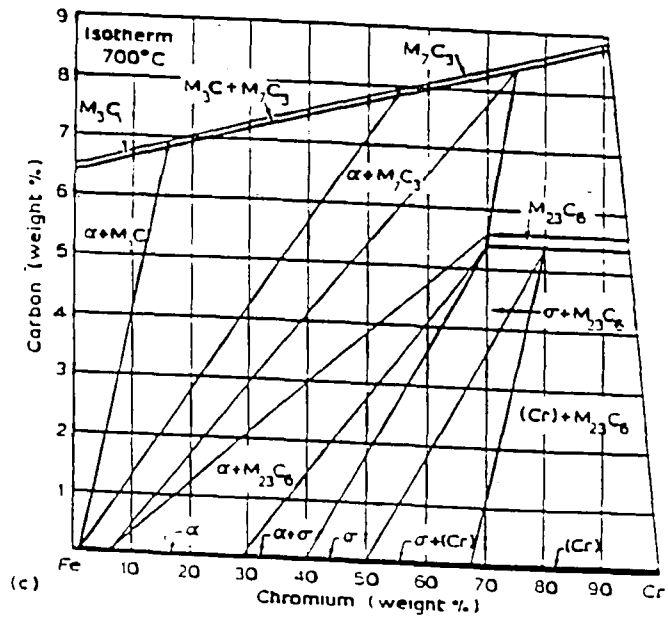

Fig. II.7 Isothermal section of the Fe-Cr-C system at 700^{0}C(reference 12).

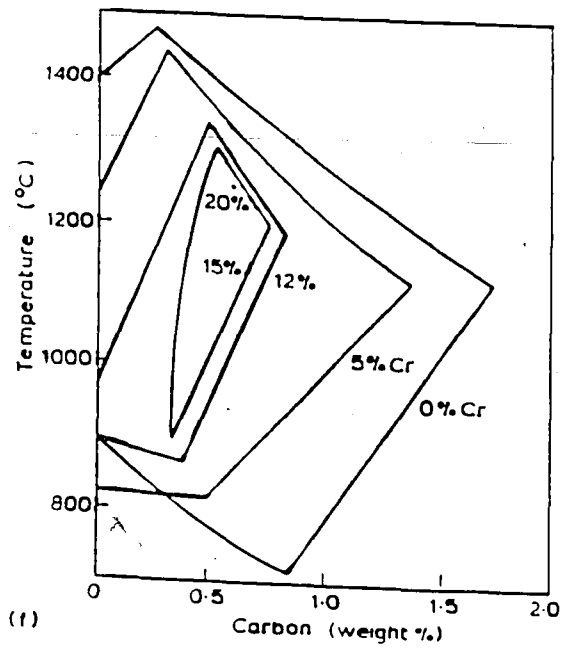

Fig. II.8 Effect of Cr additions on the temperature and carbon content of the $\gamma \rightarrow \alpha + M_3C$ eutectoid.

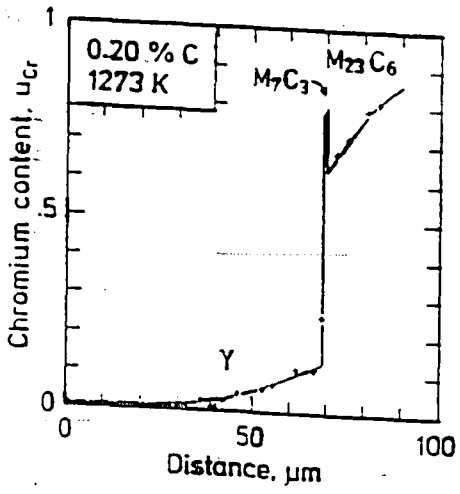

(a)

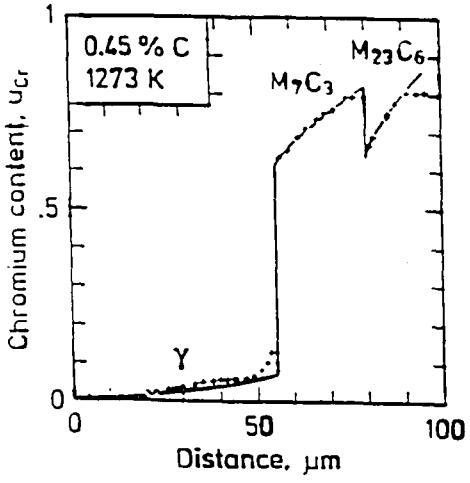

(b)

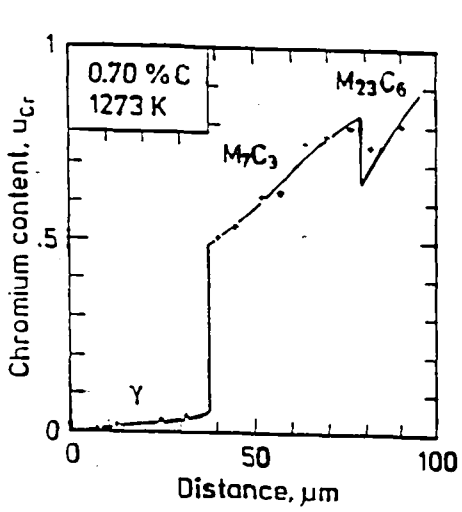

(c)

Fig. II.9 Concentration profile of the chromium in the chromized layers after 30 hours of heat-treatment. (a) 0.2% C steel (b) 0.45% C steel (c) 0.7% C steel (refernece 25).

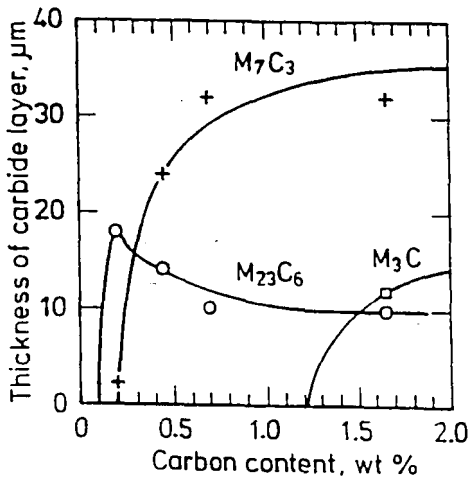

Fig. II.10 The thickness of the carbide layers after 30 hours as functions of the carbon content of the steel.

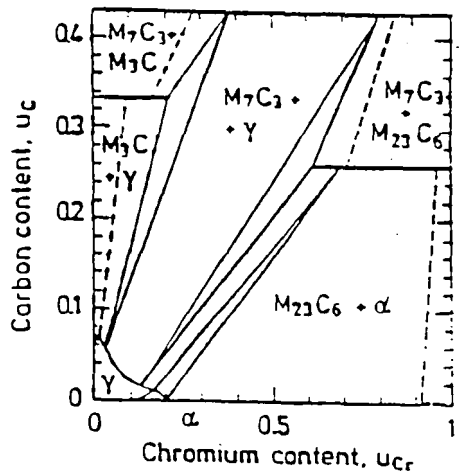

Fig. II.11 Isothermal section of the Fe-Cr-C system at 1000^{0}C.

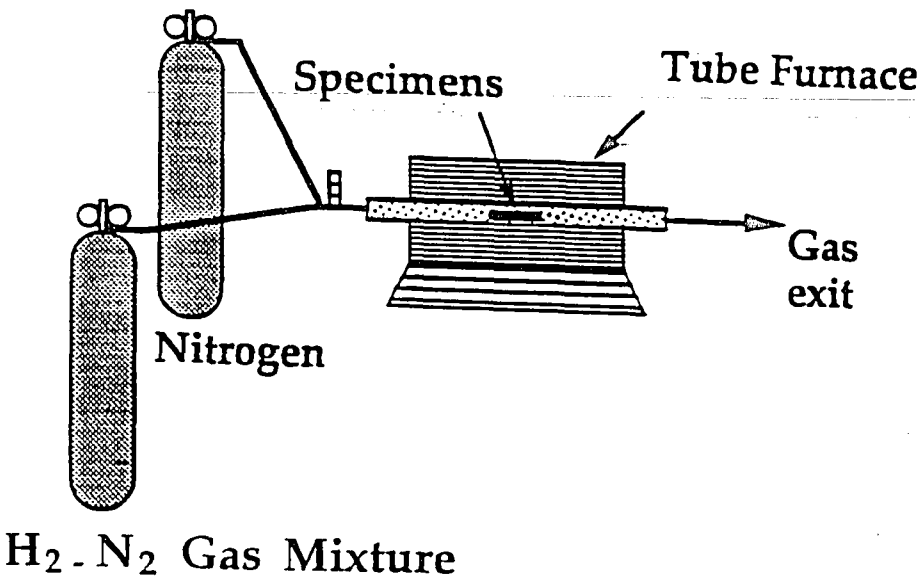

Fig. III.1 Schematic diagram of the apparatus used for decarburization.

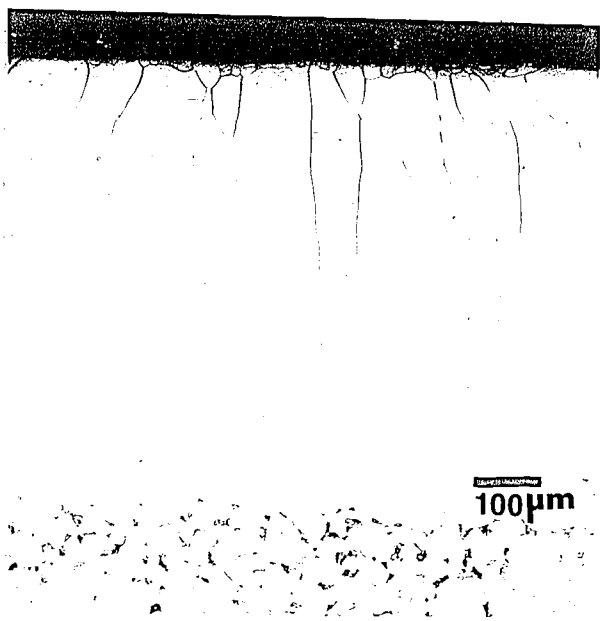

(a)

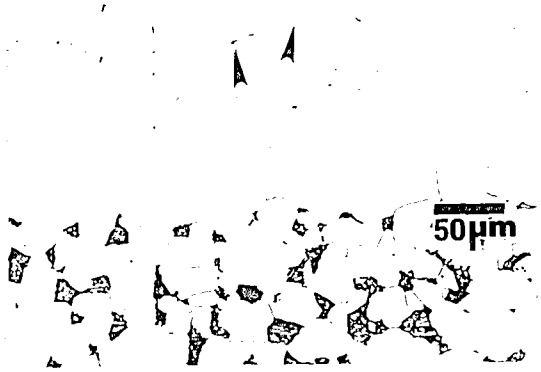

(b)

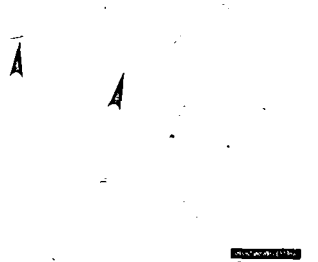

(c)

Fig. III.2 2(a) Decarburized columnar grains on the top of the substrate (LOM 100X). 2(b) (LOM 200X) and 2(c) (LOM 400X) Needle like precipitates in the decarburized columnar grains.

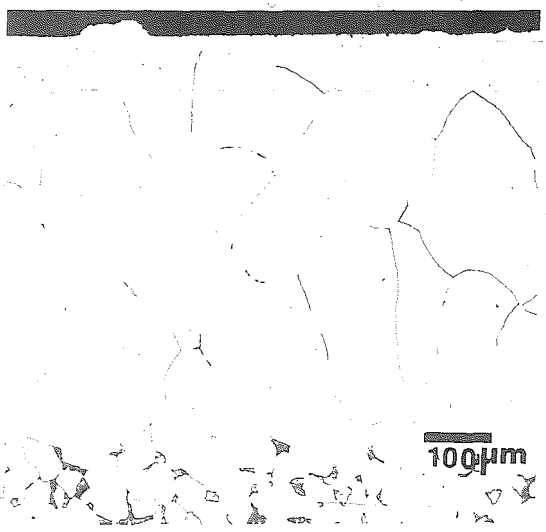

(a)

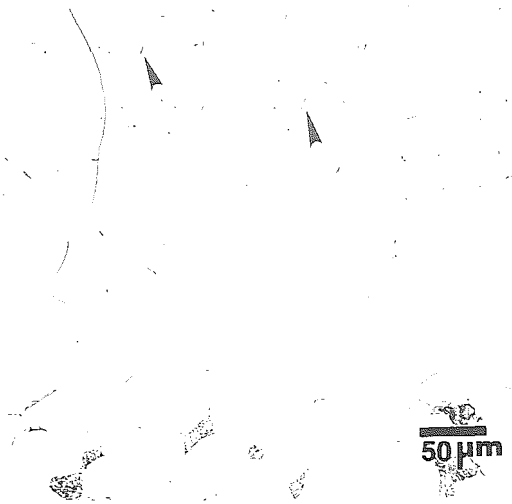

(b)

(c)

Fig. III.3 3(a) Decarburized equiaxed grains on the top of the substrate (LOM 100X). 3(b) (LOM 200X) and 3(c) (LOM 400X) Needle like precipitates in the decarburized equiaxed grains.

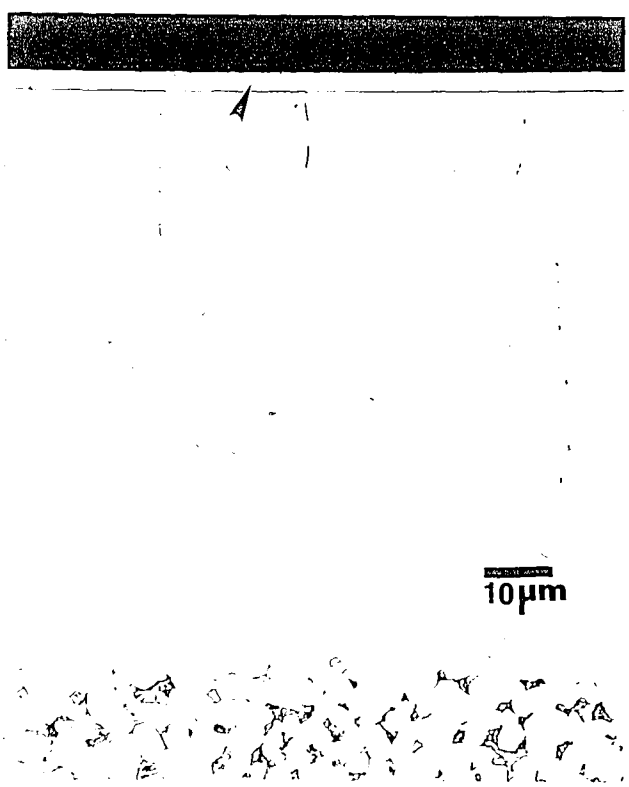

Fig. III.4 Cr layer on the top of decarburized columnar grains (LOM 100X).

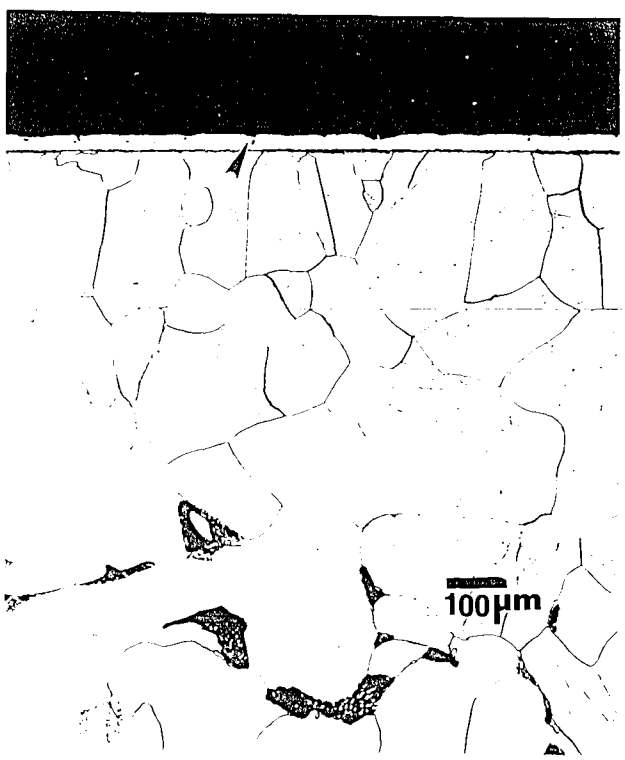

Fig. III.5 Cr layer on the top of decarburized equiaxed grains (LOM 100X).

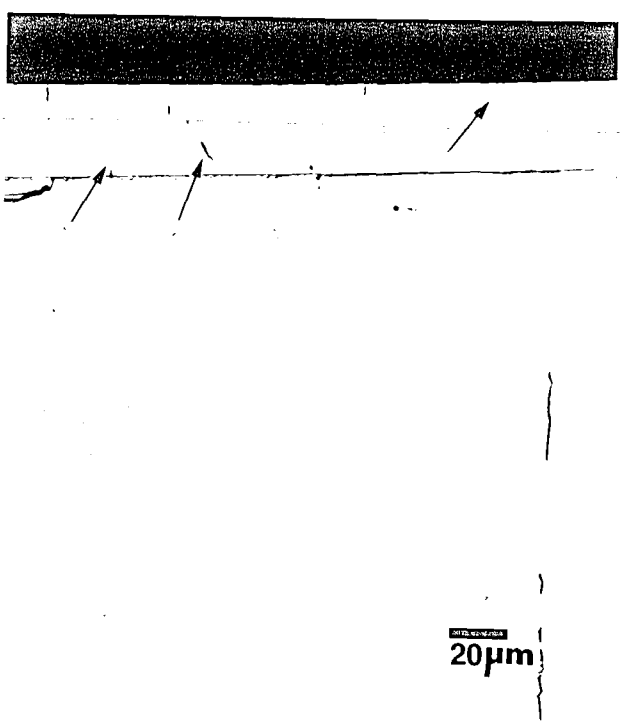

Fig. III.6 View of the chromium layer at higher magnification (LOM 500X).

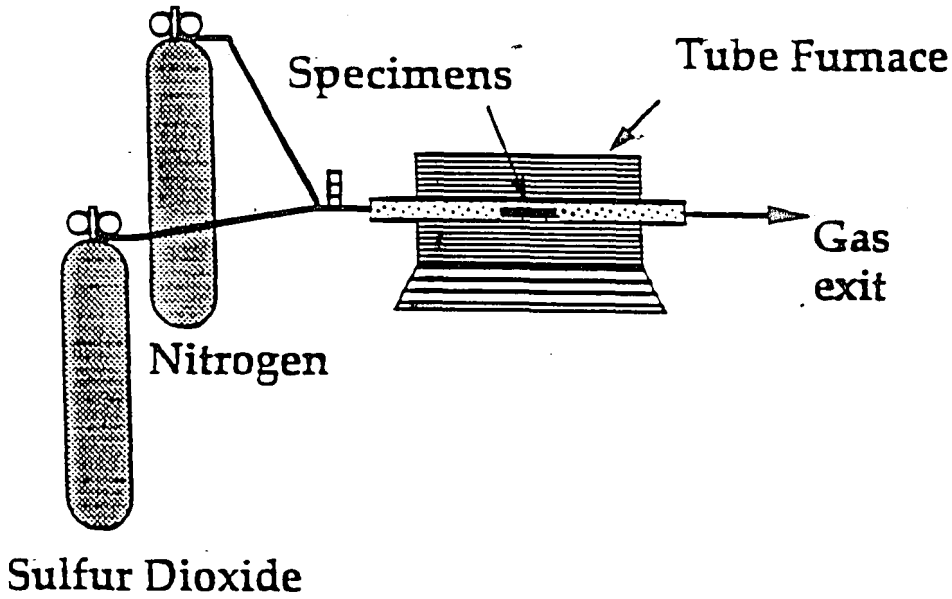

Fig. III.7 Schematic diagram of the apparatus used for sulphidation testing.

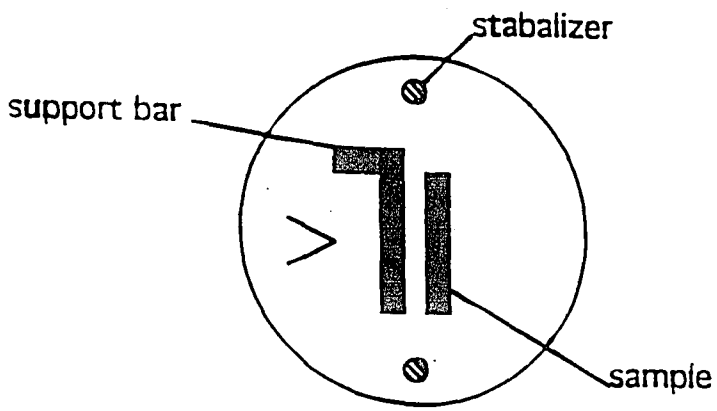

Fig. III.8 Schematic of a typical mount used in this investigation.

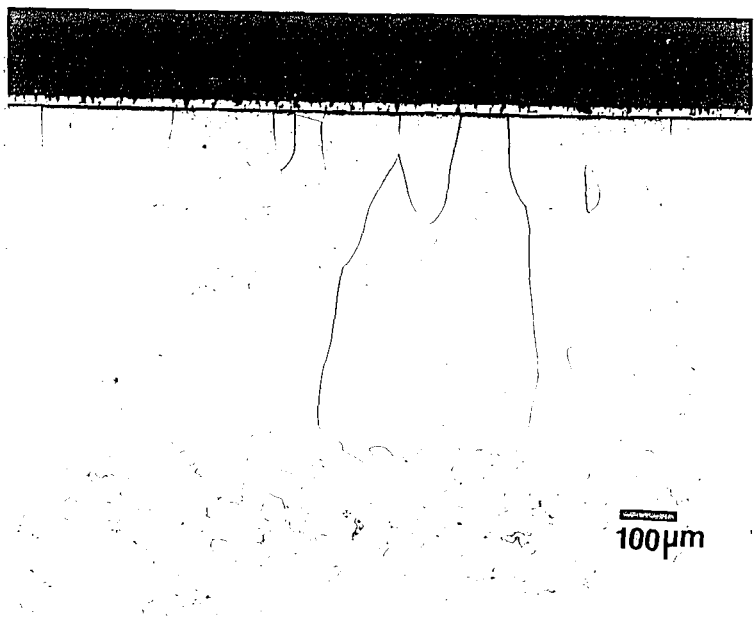

Fig. IV.1a Columnar grained microstructure after 22 hours of heat-treatment at 600^0C (LOM 100X).

Fig. IV.1b Needle like precipitates in the columnar grained microstructure after 22 hrs. of heat-treatment at 600^0C (LOM 500X).

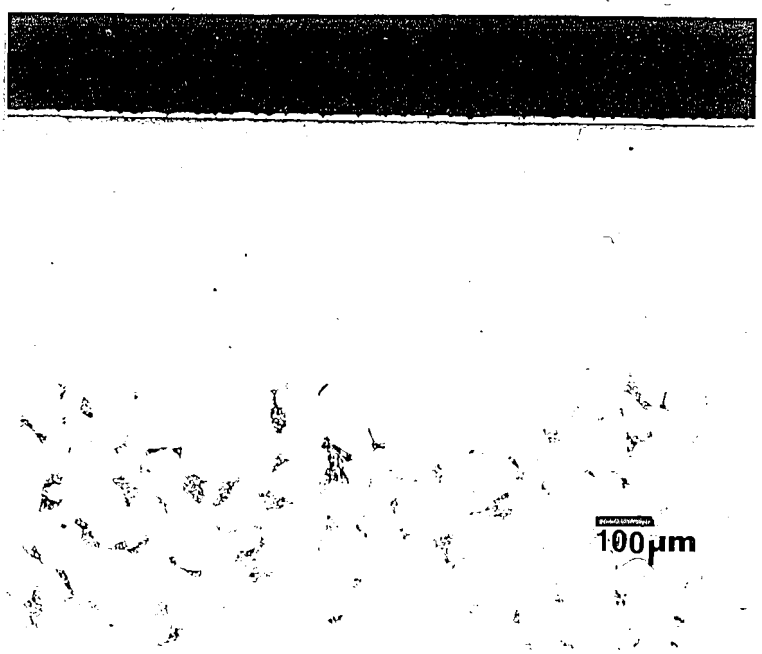

Fig. IV.2a Equiaxed grained microstructure after 22 hrs. of heat-treatment at 600^{0}C (LOM 100X).

Fig.IV.2b Needle like precipitates in the equiaxed grained microstructure after 22 hours of heat-treatment at 600^{0}C (LOM 500X).

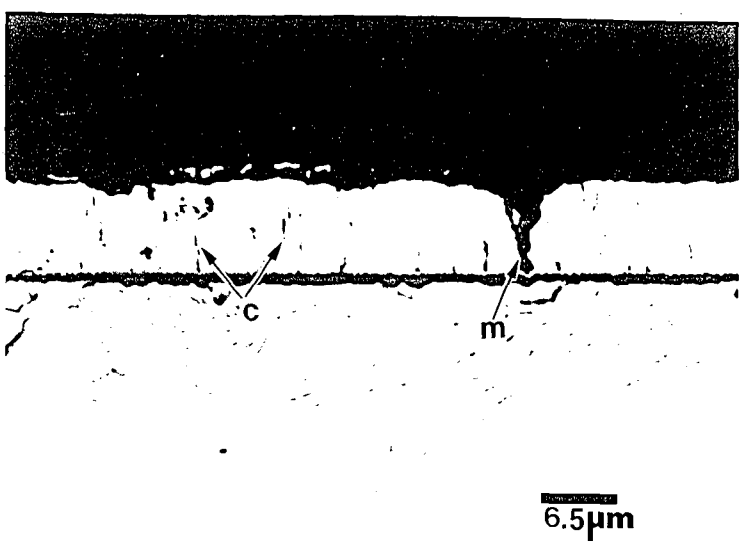

Fig. IV.3 A magnified view of the chromium layer for the sample heat-treated for 22 hours at 600^{0}C (LOM 1500X).

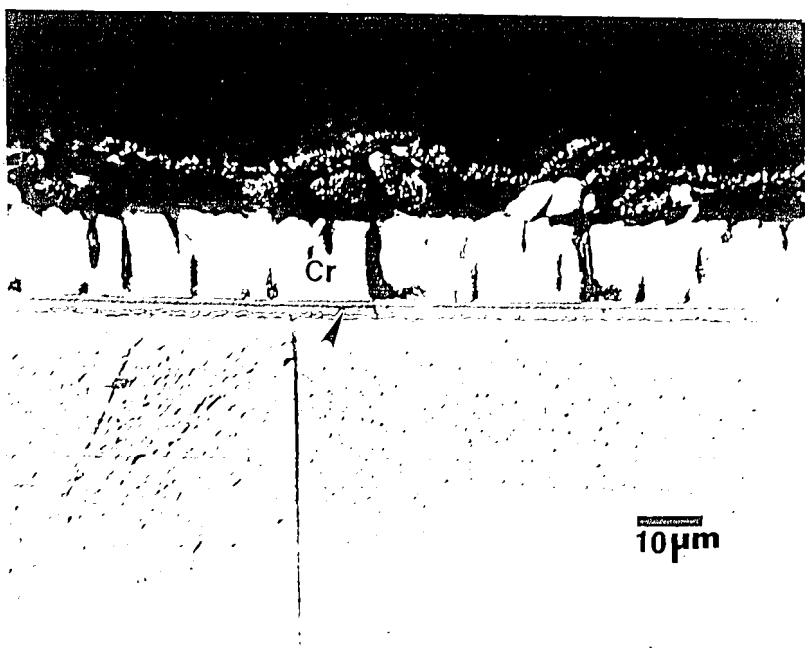

Fig. IV.4 Reaction layer below the Cr layer in the columnar sample. Sample heat-treated at 600^{0}C for 168 hrs. (LOM 1000X).

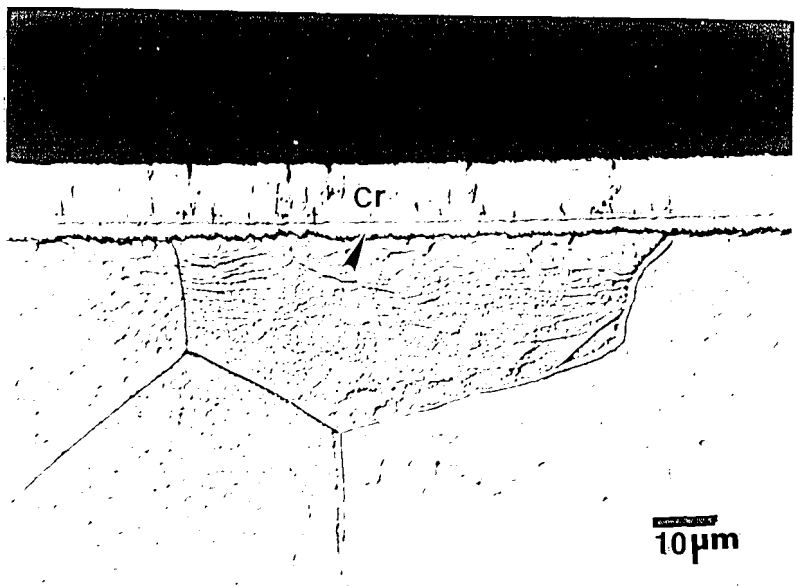

Fig. IV.5 Reaction layer below the Cr layer in the equiaxed sample. Sample heat-treated at 600^{0}C for 168 hrs. (LOM 1000X).

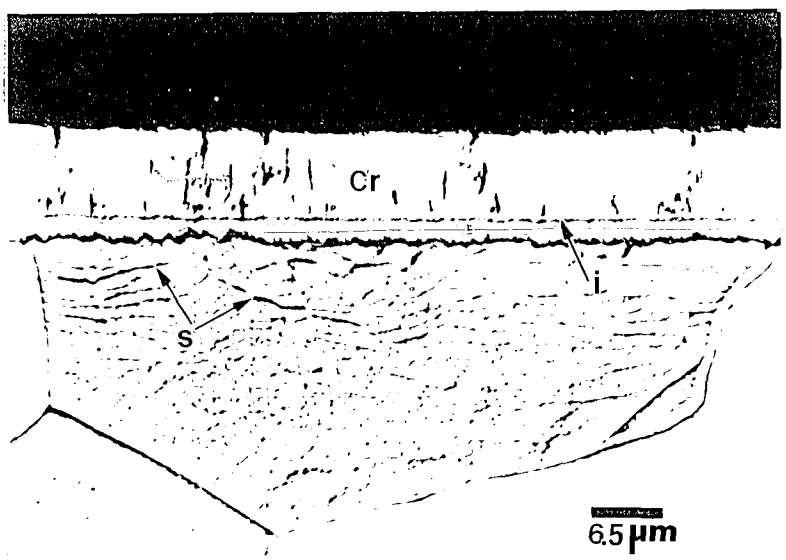

Fig. IV.6 A magnified view of the reaction layer below the chromium layer (LOM 1500X).

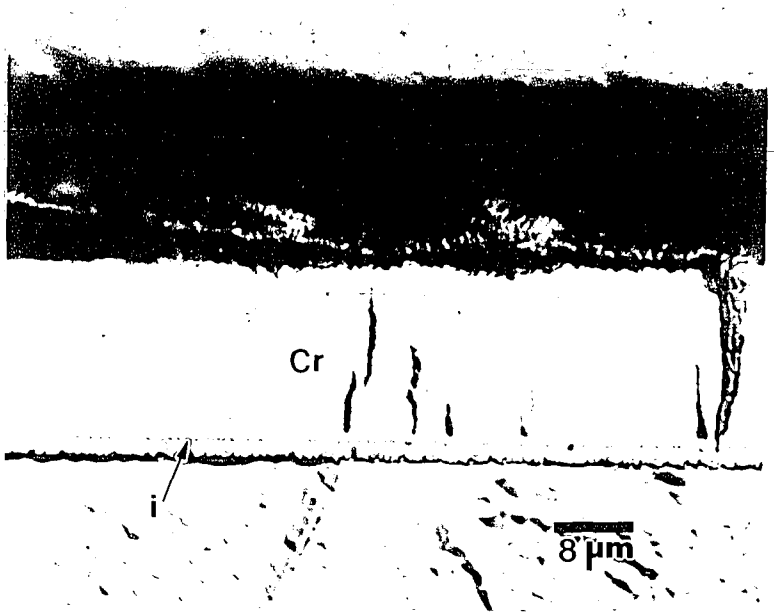

Fig. IV.7 Reaction layer below the chromium layer after 500 hours of heat-treatment at 600°C (LOM 1200X).

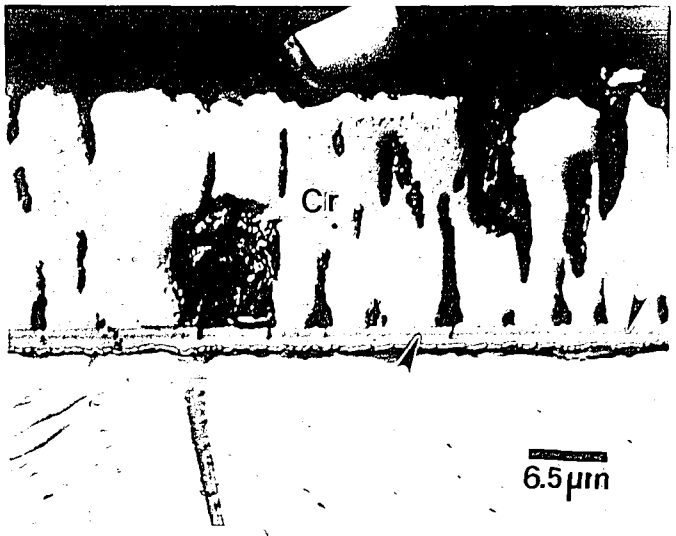

(a)

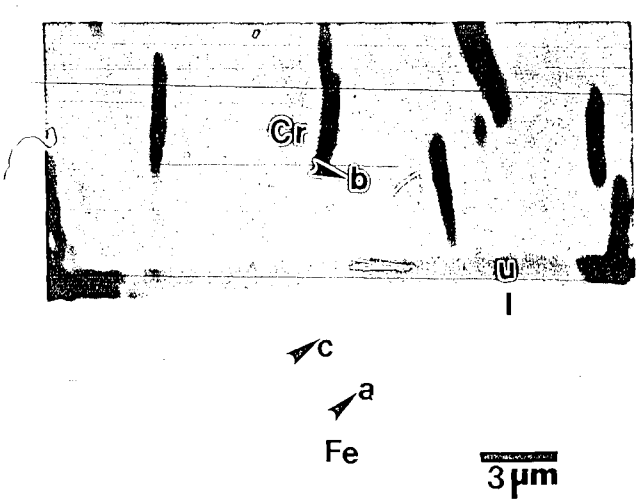

(b)

(c)

Fig. IV.8 (a) View of the reaction layer showing two layers (arrow indicates the interface between the two layers). Picture taken by Nomarski Interference Contrast technique (LOM 1500X). (b) Backscattered image (15KV) showing the reaction layer (arrow marked u indicates the upper layer and l indicates the lower layer). (c) Seconadry electron image of the same area as in b (3600X).

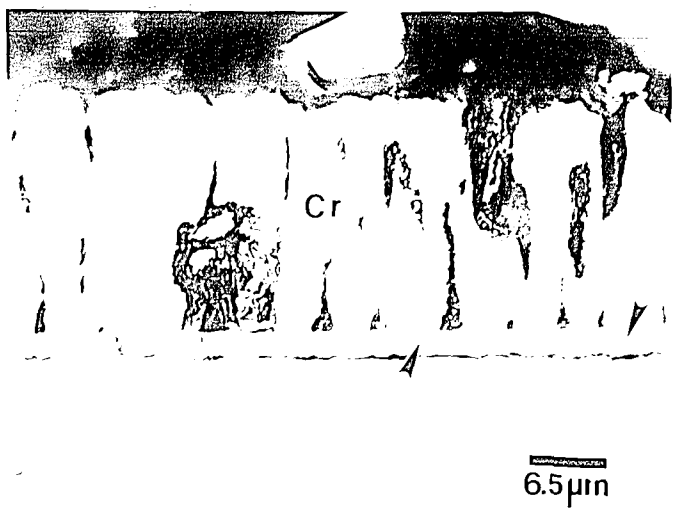

(a)

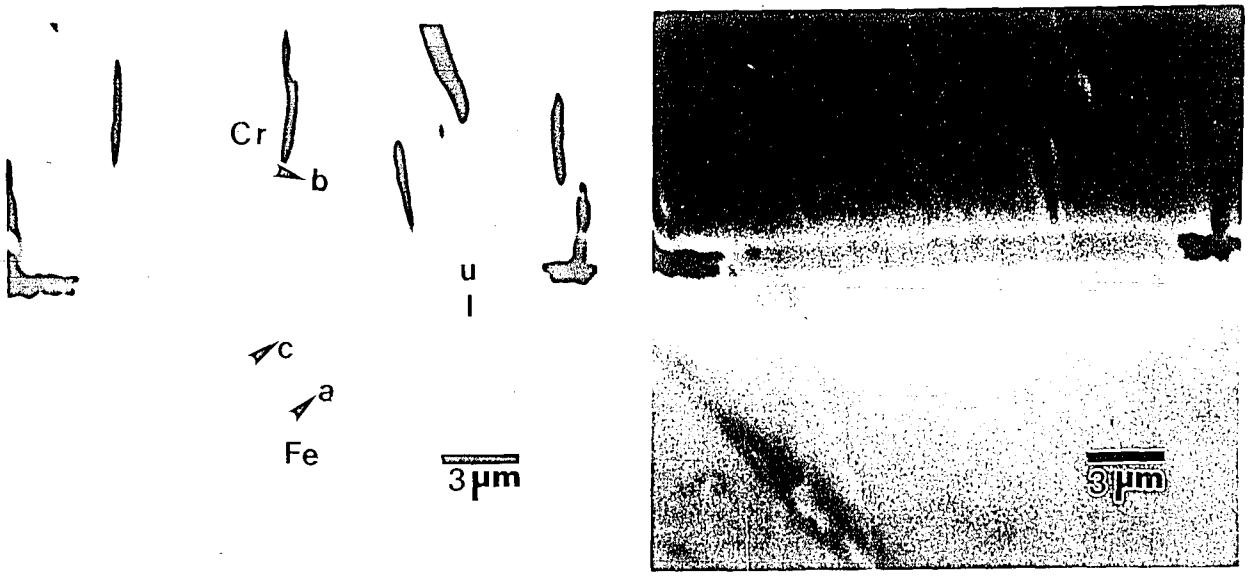

(b) (c)

Fig. IV.8 (a) View of the reaction layer showing two layers (arrow indicates the interface between the two layers). Picture taken by Nomarski Interference Contrast technique (LOM 1500X). (b) Backscattered image (15KV) showing the reaction layer (arrow marked u indicates the upper layer and l indicates the lower layer). (c) Seconadry electron image of the same area as in b (3600X).

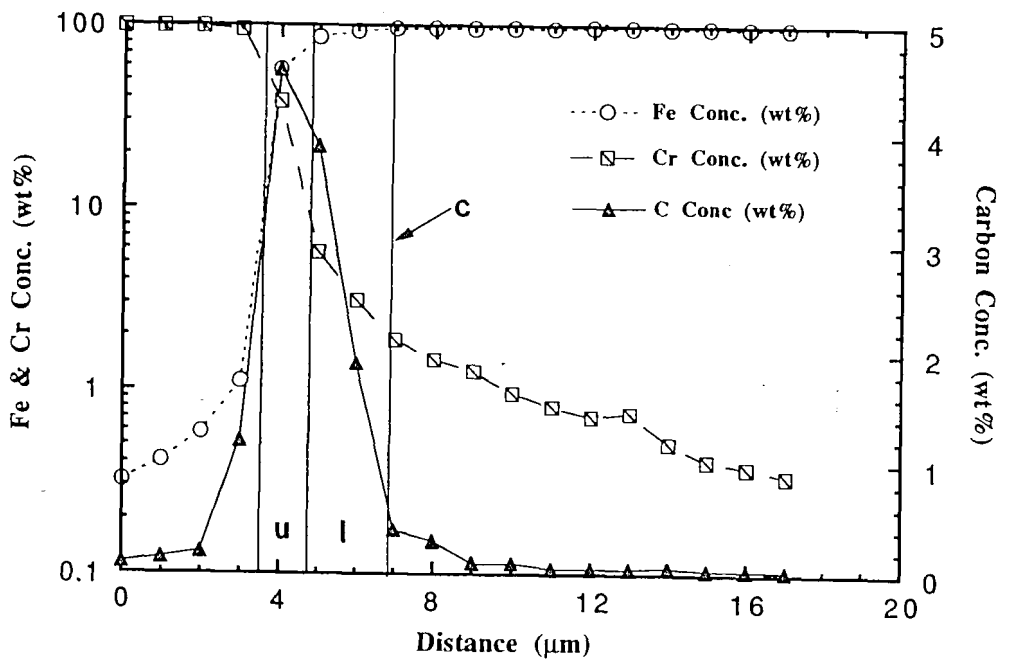

Fig. IV.9 Concentration profiles of Fe, Cr and C from chromium layer (point b in fig. IV.8b) into the decarburized layer (point a in fig. IV.8b).

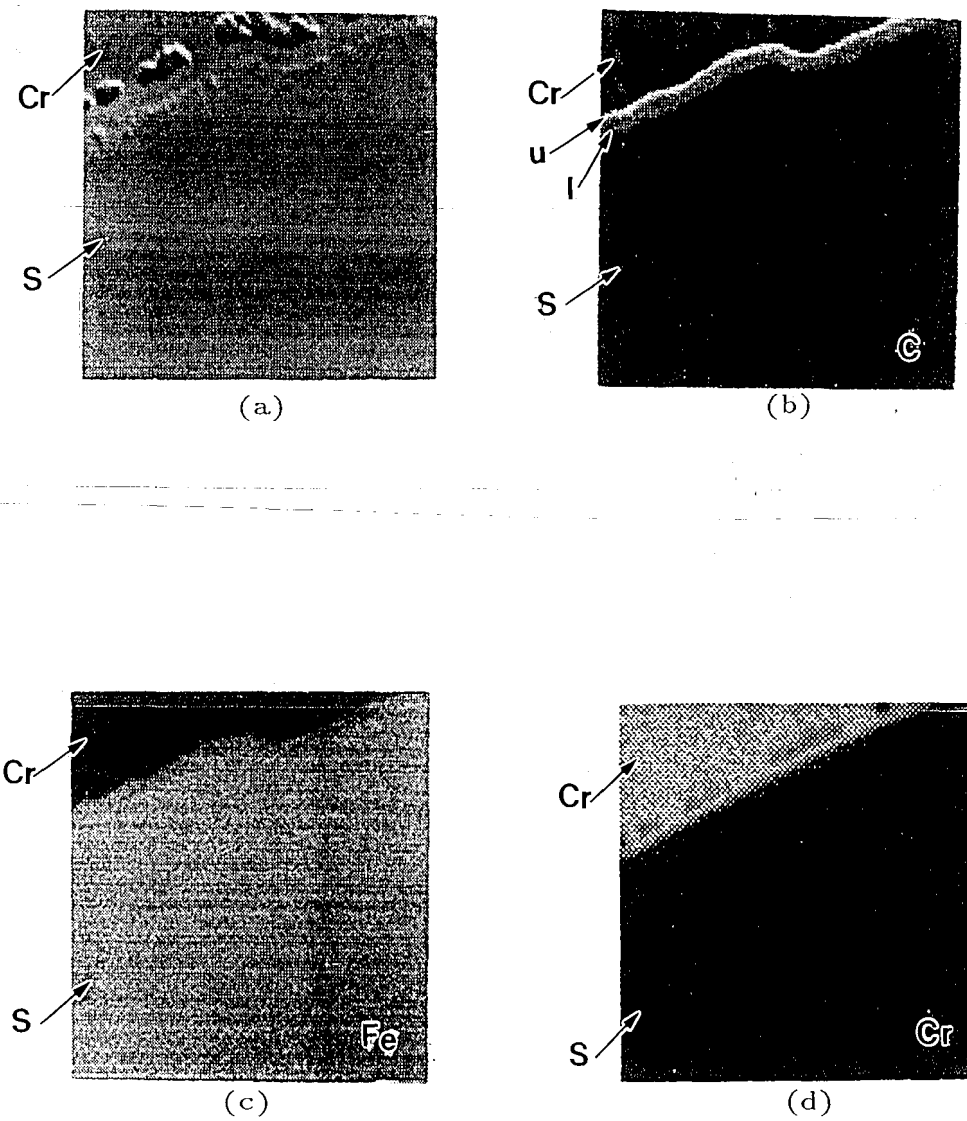

Fig. IV.10 WDS X-ray maps. 10a-secondary electron image (2000X). Arrows marked; Cr indicates the chromium layer, u indicates the upper layer in reaction layer, l indicates lower layer in reaction layer and S indicates the substrate. 10b-carbon map, 10c-Fe map, 10d-Cr map.

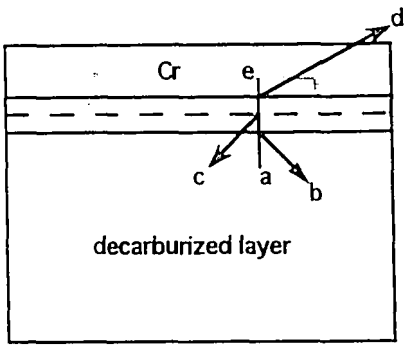

(a)

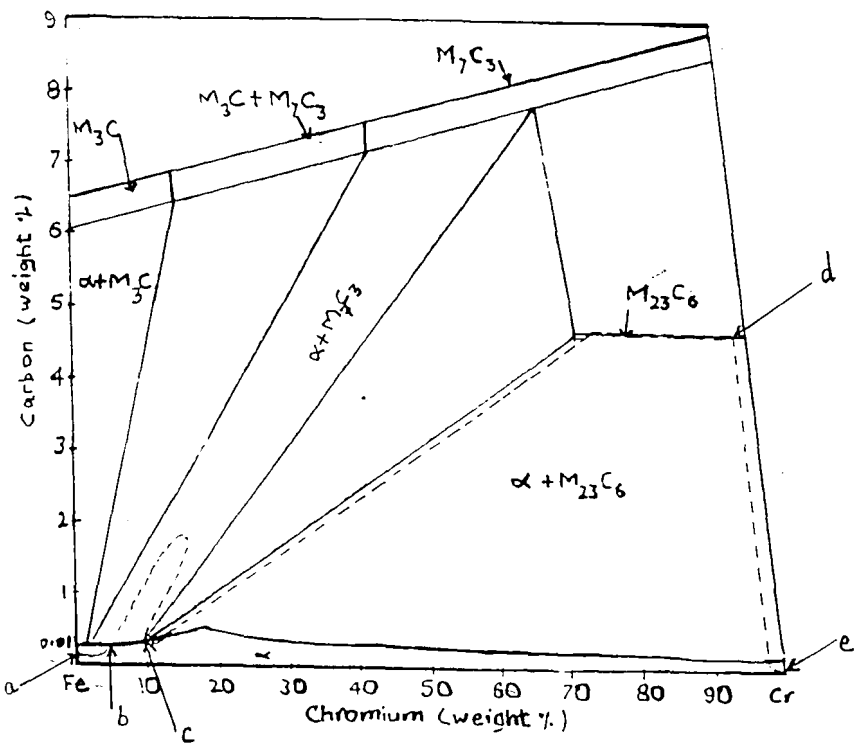

(b)

Fig. IV.11 (a) Schematic of the diffusion path (b) Possible diffusion path (shown by dashed lines in the ternary phase diagram) from the decarburized layer into the Cr layer through the reaction layer.

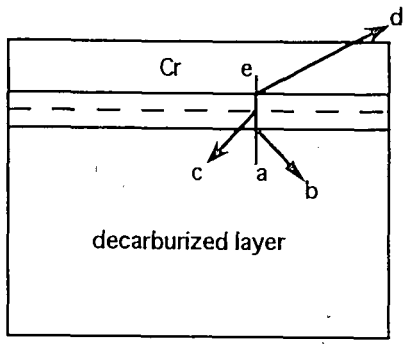

(a)

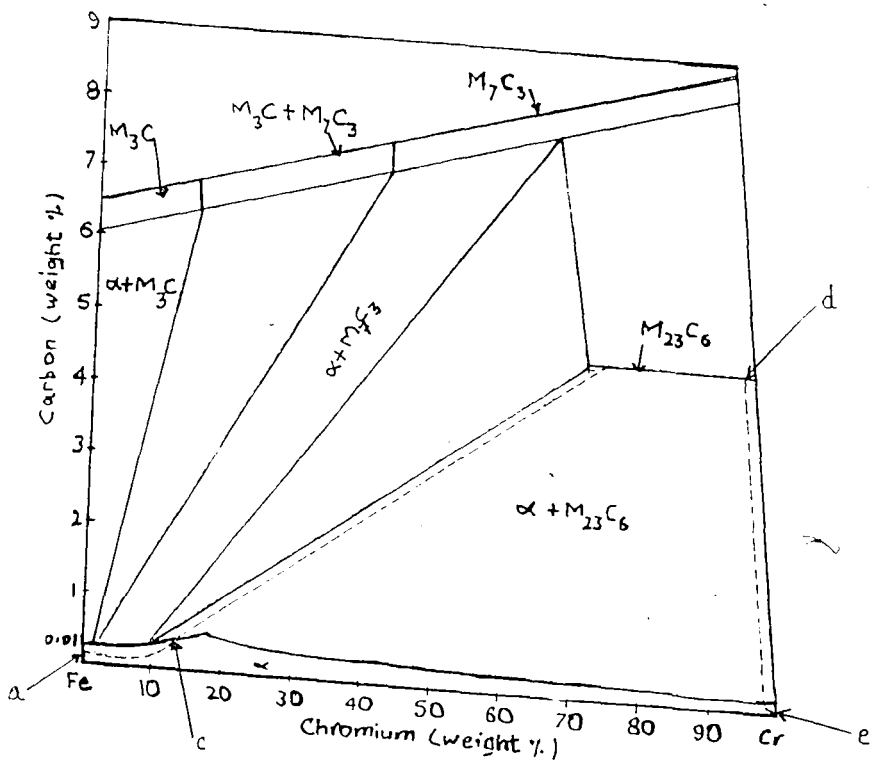

(b)

Fig. IV.12 (a) Schematic of the diffusion path (b) Possible diffusion path (shown by dashed lines in the ternary phase diagram) from the decarburized layer into the Cr layer through the reaction layer.

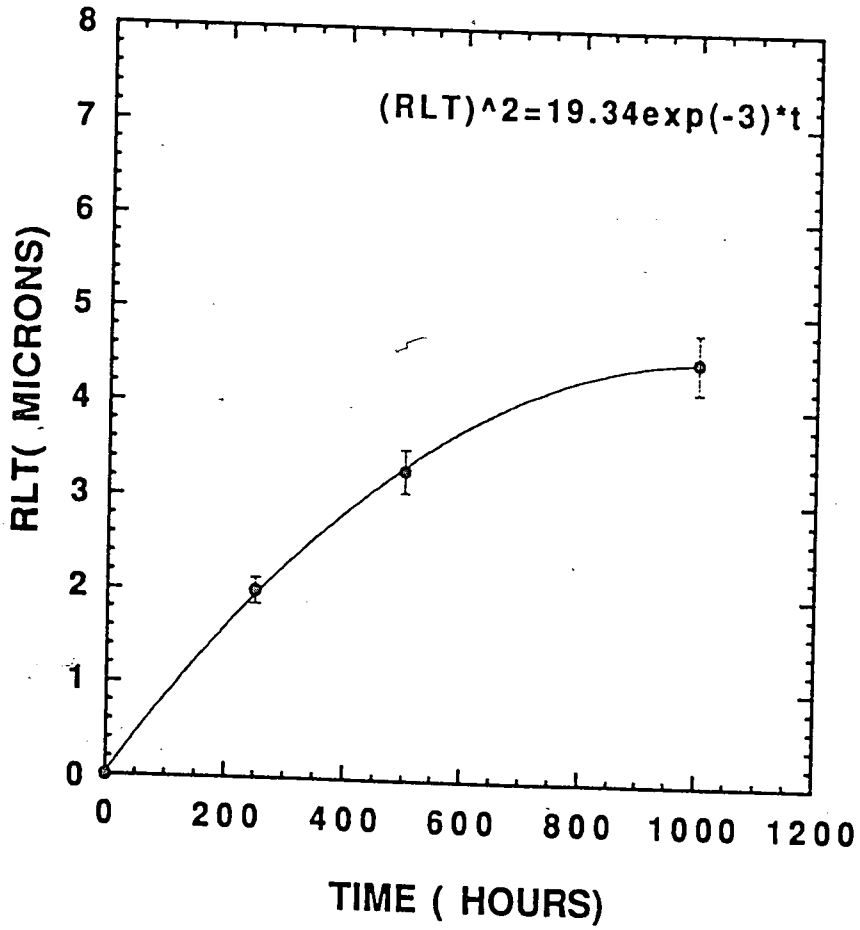

Fig. IV.13 Reaction Layer Thickness (RLT) vs Time plot.

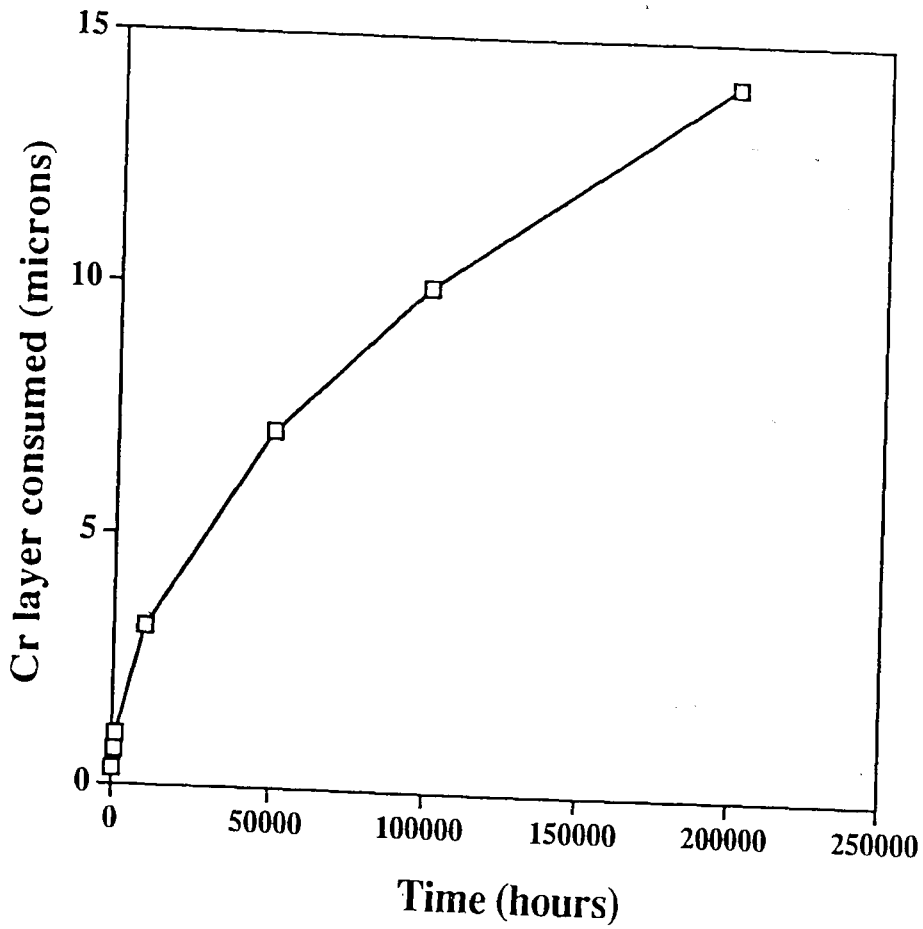

Fig. IV.14 Plot of Cr layer consumed (microns) vs time (hours).

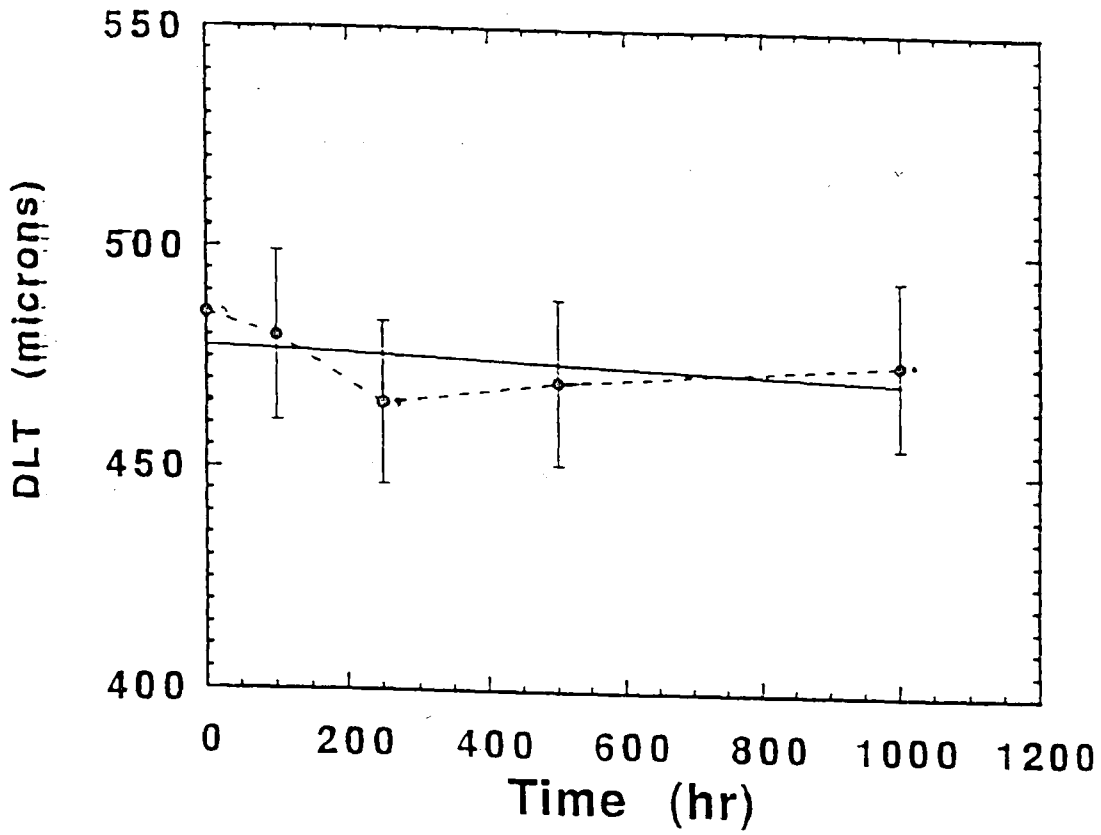

Fig. IV.15 Decarburized Layer Thickness (DLT) vs Time plot.

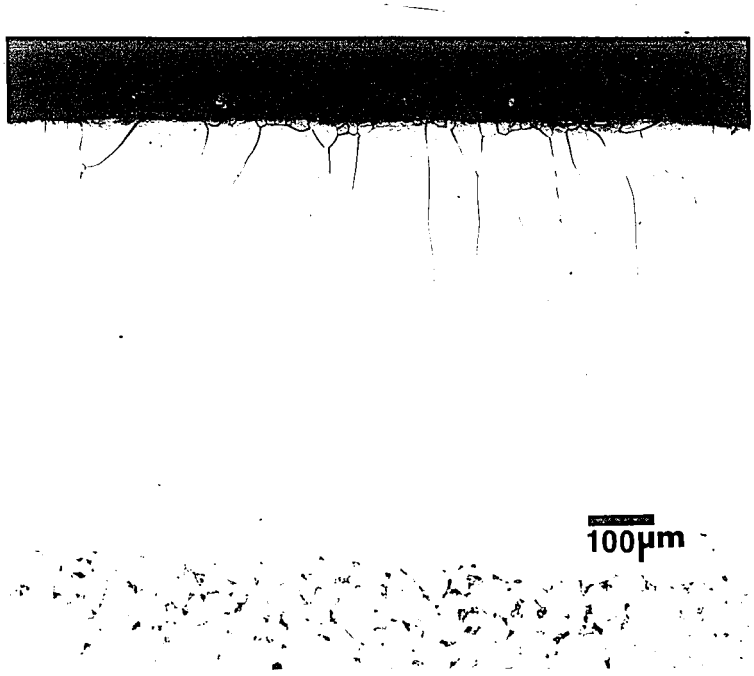

Fig. IV.16 Decarburized columnar grains above the substrate containing ferrite and pearlite (LOM 100X).

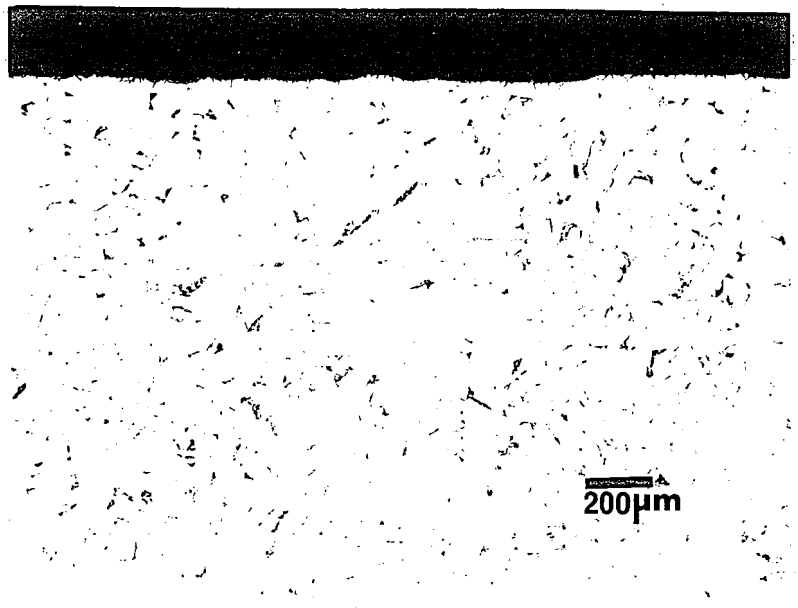

(a)

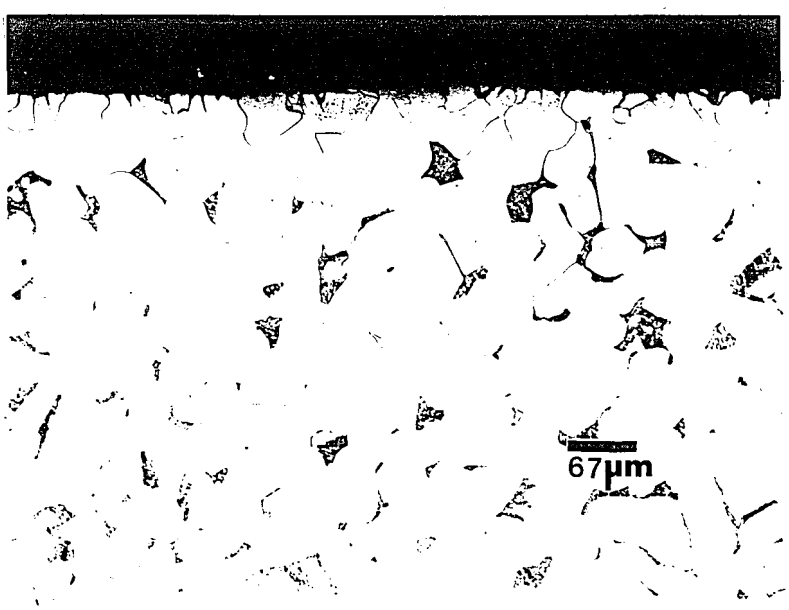

(b)

Fig. IV.17 Microstructure after 4 hours of heat-treatment at 1000^{0}C (no Cr layer) showing the redistribution of carbon (a) LOM 50X (b) LOM 150X.

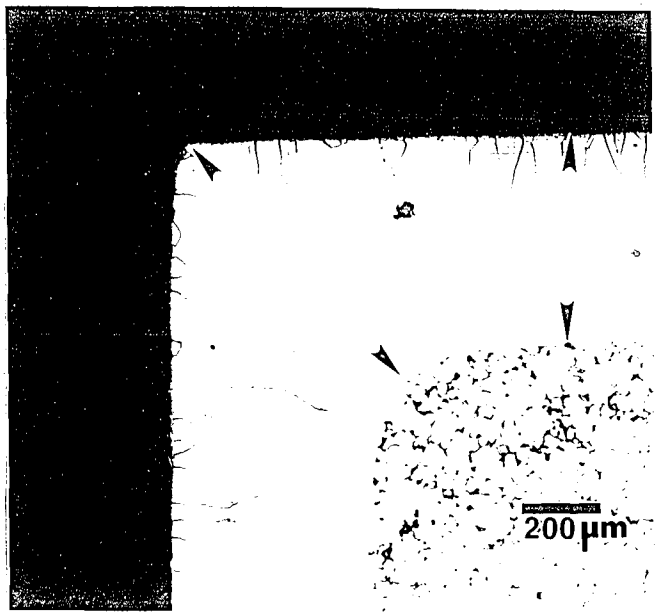

Fig IV.18 Microstructure showing higher thickness of the decarburized layer at the corners (before electroplating or chromizing heat-treatment). (LOM 50X).

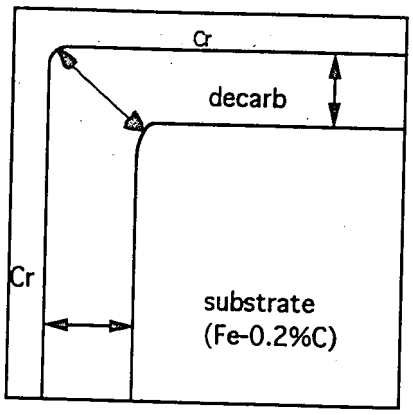

(a)

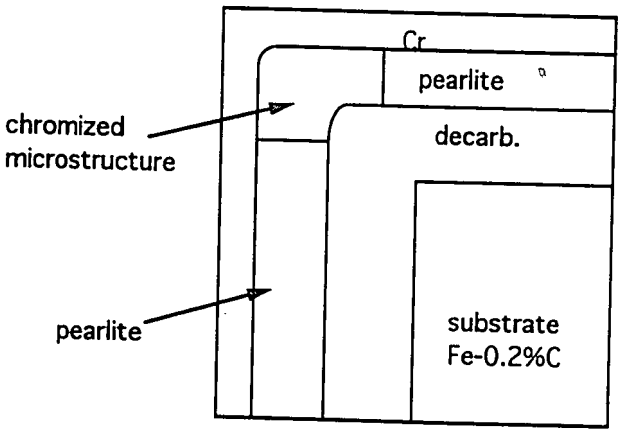

(b)

Fig. IV.19 (a) Schematic of the macrostructure near the corners before the heat-treatment. (b) Schematic of the macrostructure after the heat-treatment at 1000^{0}C for 4 hours. In (a) and (b) Cr indicates the Cr layer at the top and decarb indicates the decarburized layer.

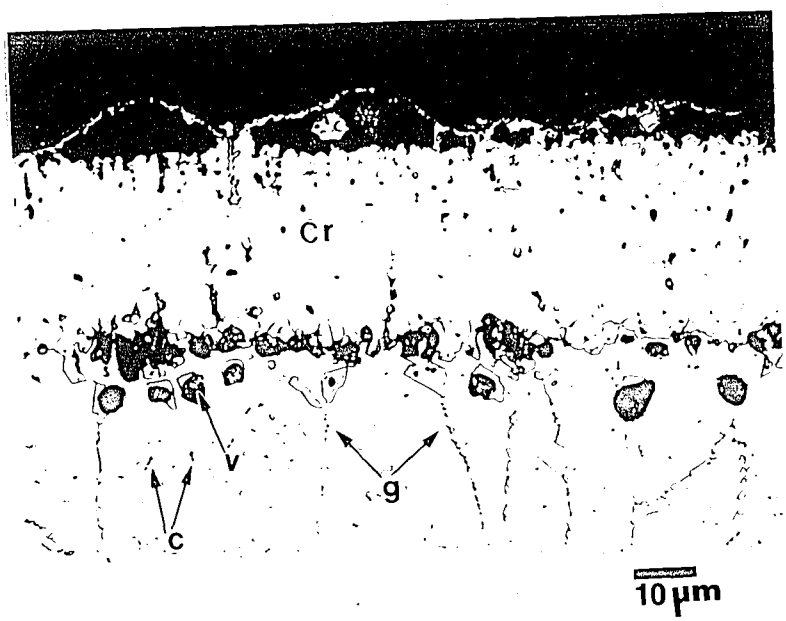

(a)

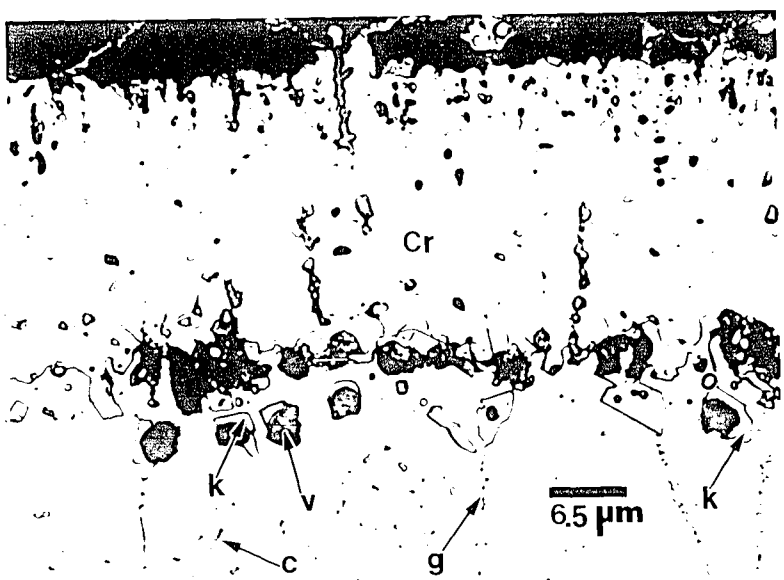

(b)

Fig. IV.20 Coating microstructure after 4 hours of heat-treatment at 1000°C. (a) LOM 1000X (b) magnified view featuring voids and porosity in the coating. (LOM 1500X).

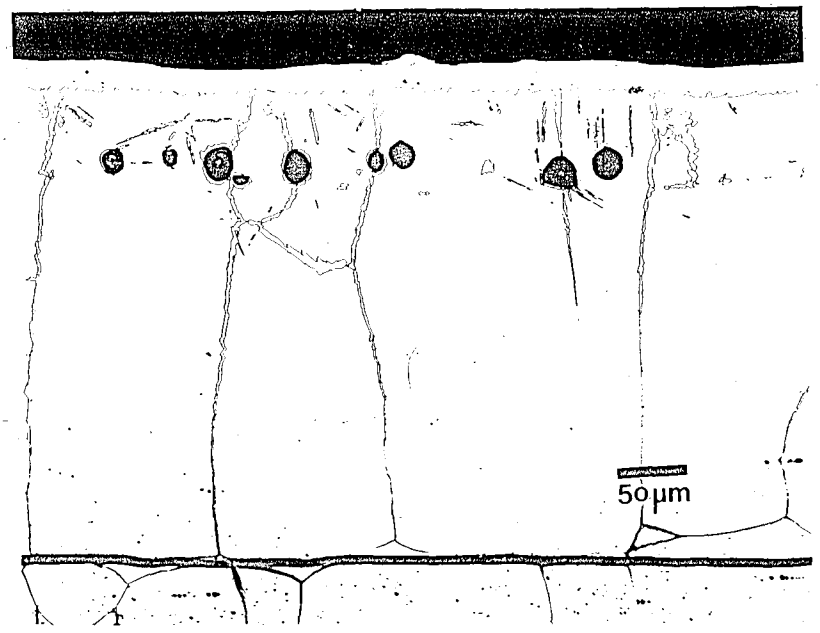

(a)

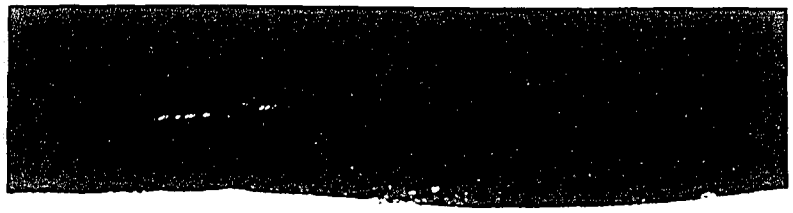

(b)

Fig. IV.21 Typical microstructure of the chromized coating. (a) LOM 200X (b) microstructure featuring voids and porosity in the coating (LOM 500X). (courtesy Brian J. Smith).

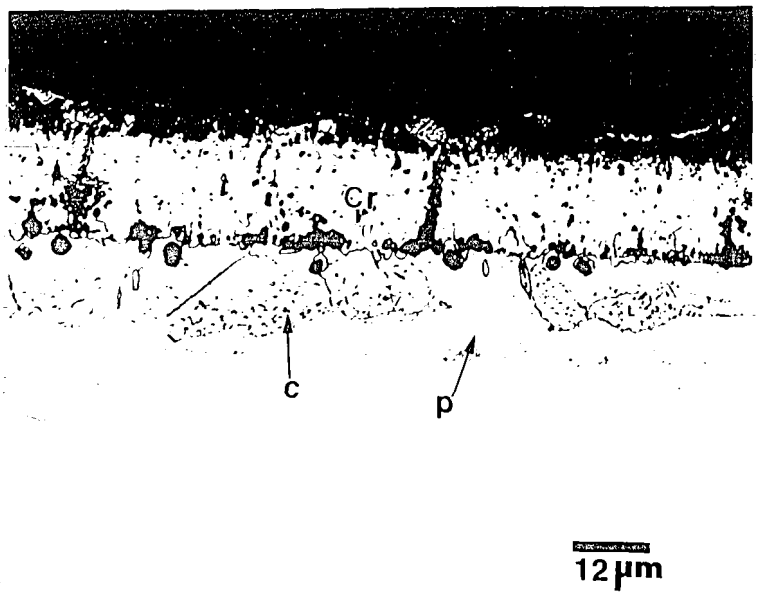

Fig. IV.22 View of the coating showing carbides (marked c) and pearlite (marked p) that could not be resolved (LOM 800X).

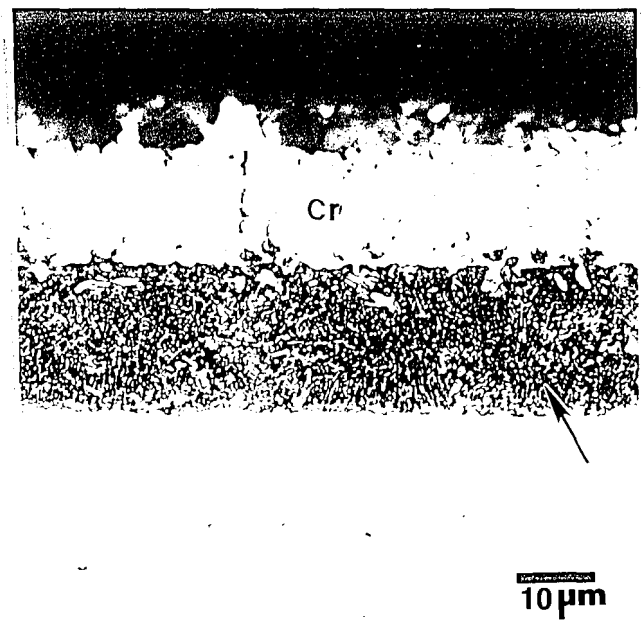

(a)

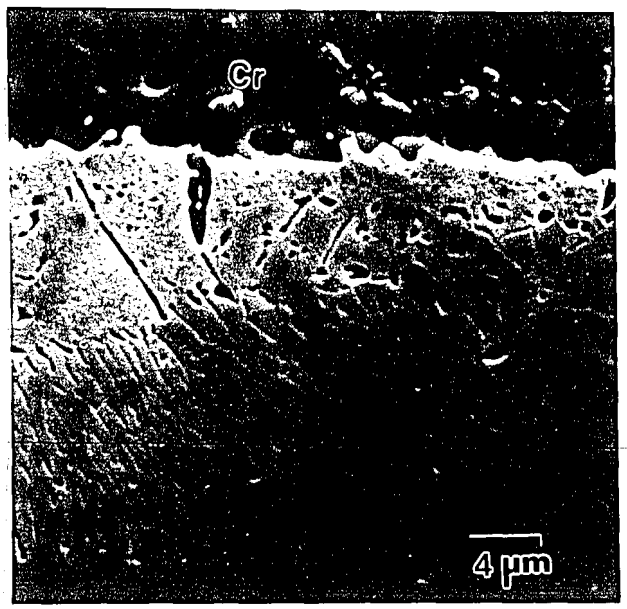

(b)

Fig. IV.23 (a) Microstructure showing pearlite in the coating (LOM 1000X). (b) View of the pearlitic layer at higher magnification (SEM 2500X)

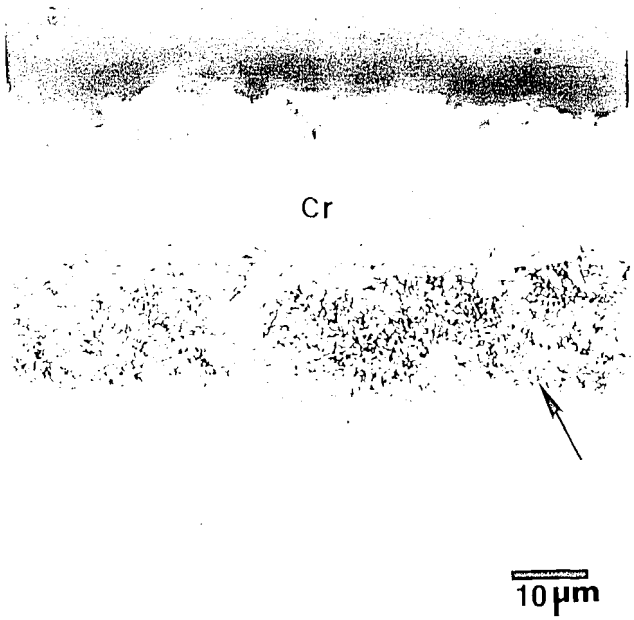

(a)

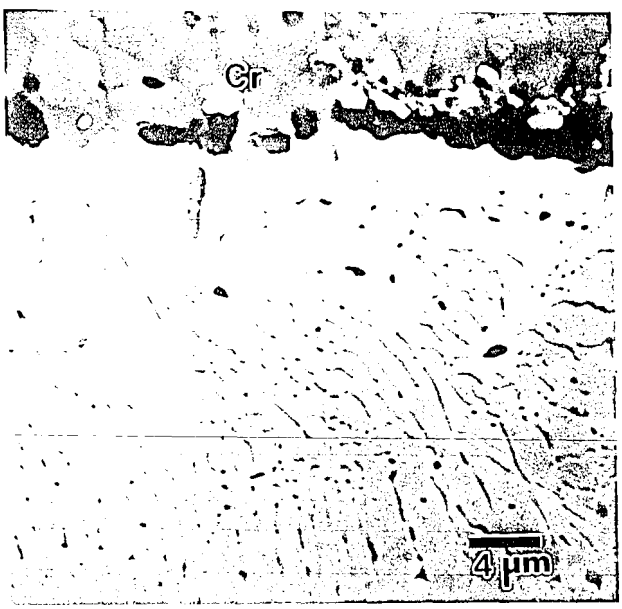

(b)

Fig. IV.23 (a) Microstructure showing pearlite in the coating (LOM 1000X). (b) View of the pearlitic layer at higher magnification (SEM 2500X)

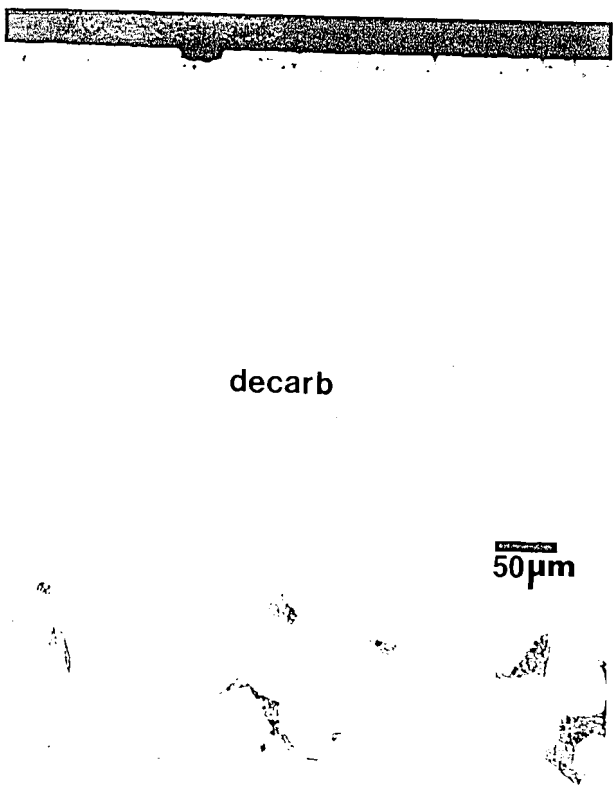

Fig. IV.24 Microstructure showing the equiaxed grained decarburized layer (marked decarb) below the coating after chromizing simulation heat-treatment.(LOM 200X).

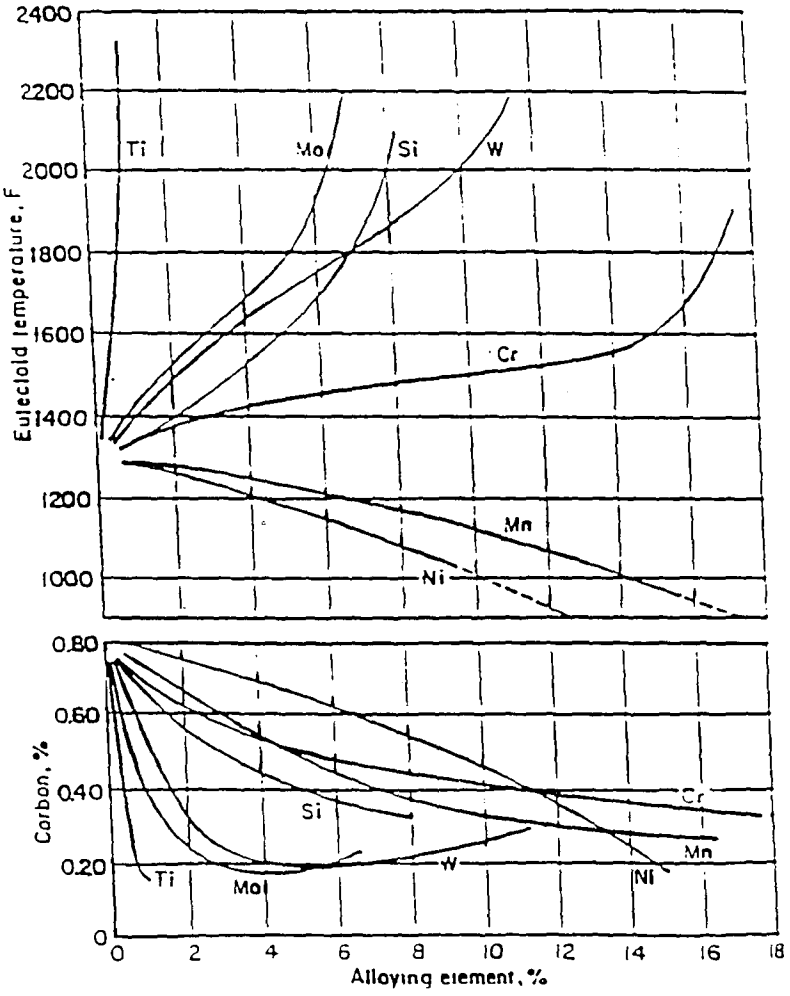

Fig. IV.25 Eutectoid composition and eutectoid temperature, as influenced by several alloying elements (reference 41).

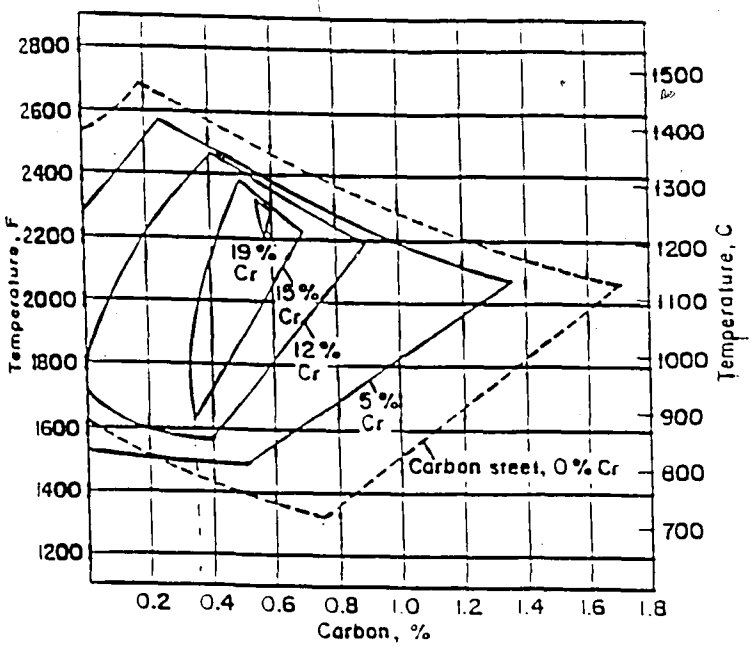

Fig. IV.26 Effect of several uniform chromium contents on the carbon limitations for pure austenite at elevated temperatures (reference 41).

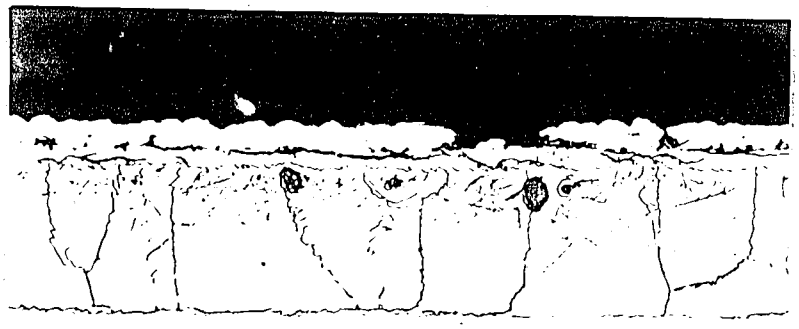

10µm

(a)

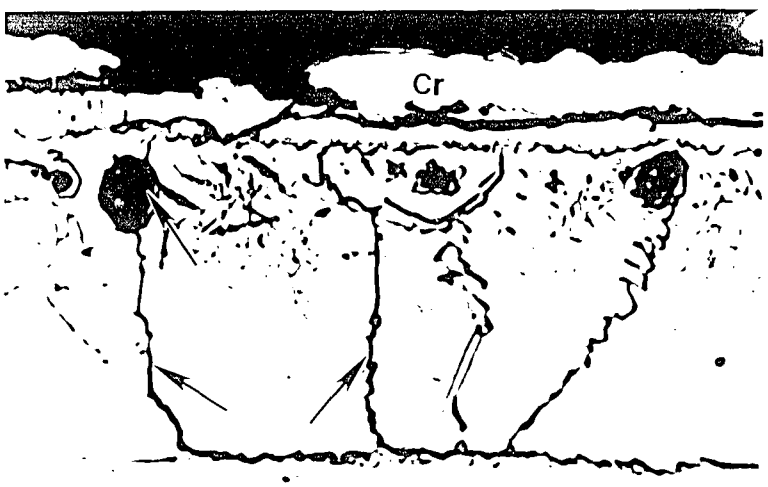

(b)

Fig. IV.27 Micrograph of the chromized layer induced below the Cr layer after 1 1/2 hours of heat-treatment at 1000^0C.(a) LOM 1000X (b) LOM 2000X

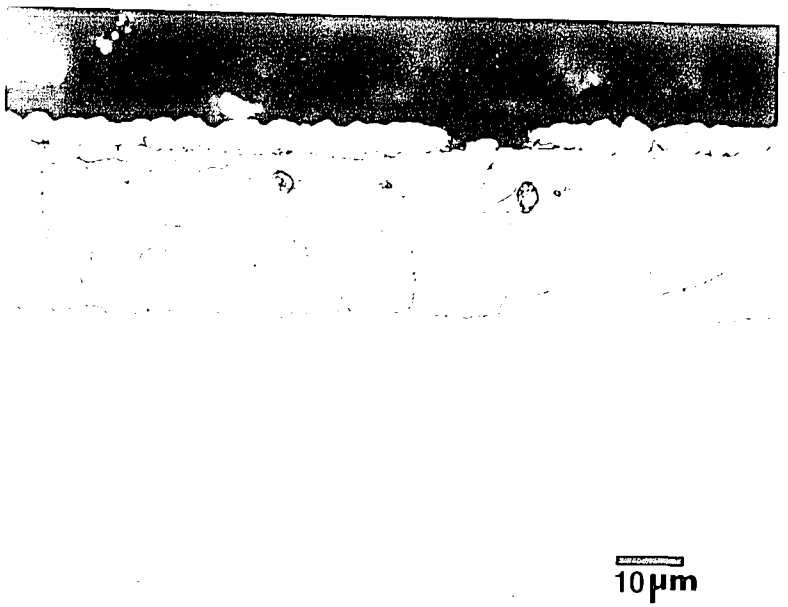

(a)

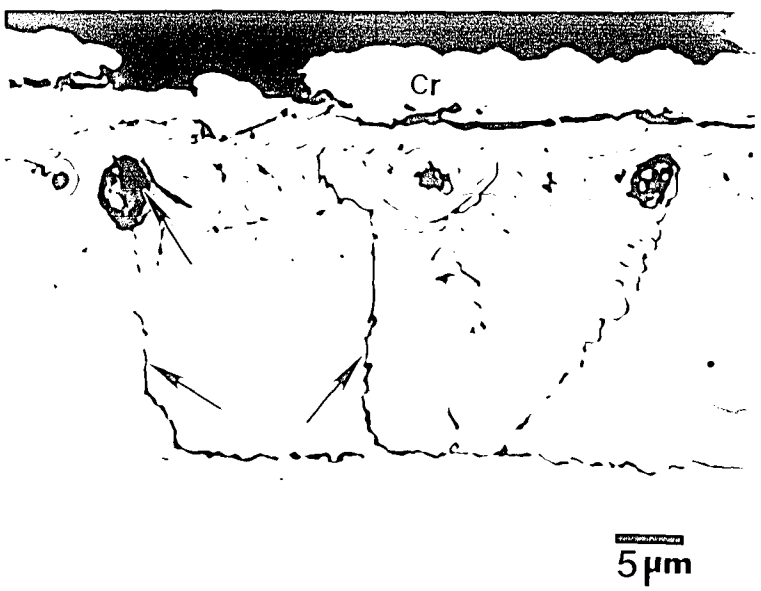

(b)

Fig. IV.27 Micrograph of the chromized layer induced below the Cr layer after 1 1/2 hours of heat-treatment at 1000^{0}C.(a) LOM 1000X (b) LOM 2000X

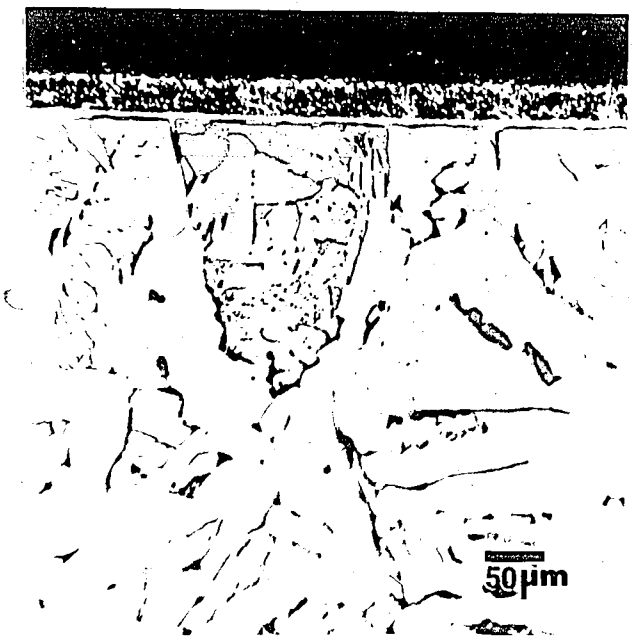

(a)

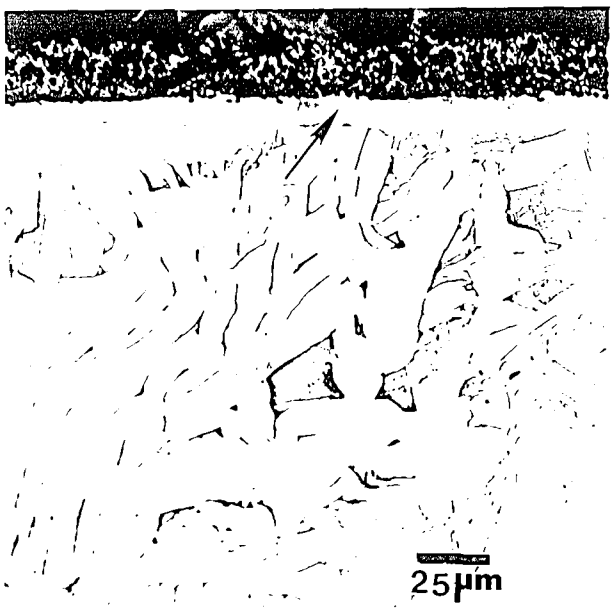

(b)

Fig. IV.28 Microstructure of the quenched sample after heat-treatment at 1000^{0}C showing the bainitic microstructure. (a) LOM 200X (b) LOM 400X

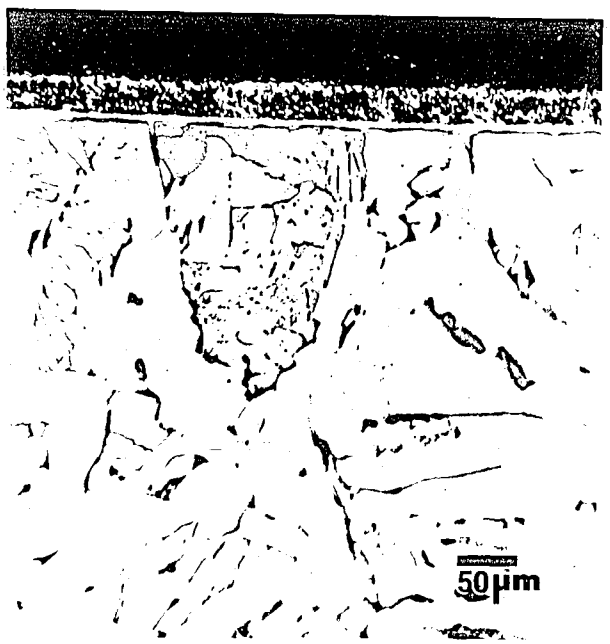

(a)

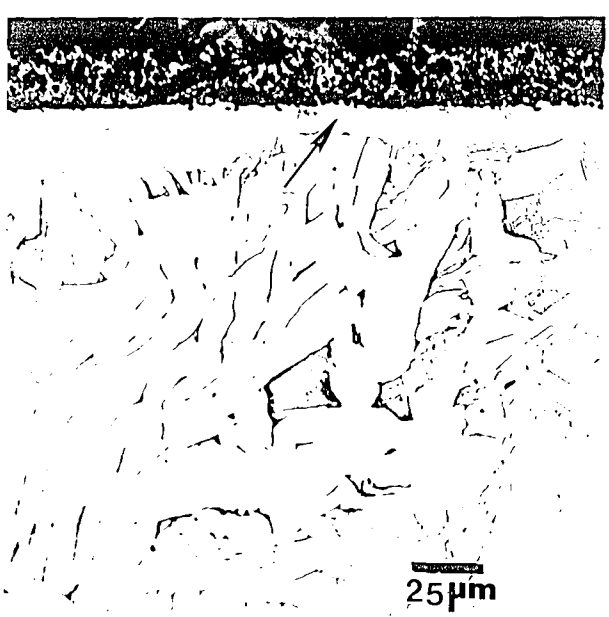

(b)

Fig. IV.28 Microstructure of the quenched sample after heat-treatment at 1000^{0}C showing the bainitic microstructure. (a) LOM 200X (b) LOM 400X

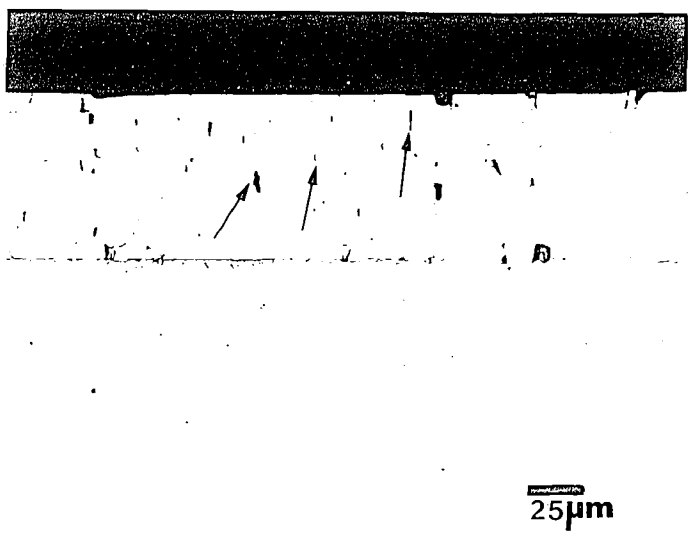

Fig. IV.29 Microstructure of the as plated Cr layer above the substrate (arrows indicate microcracks in the Cr layer) (LOM 400X).

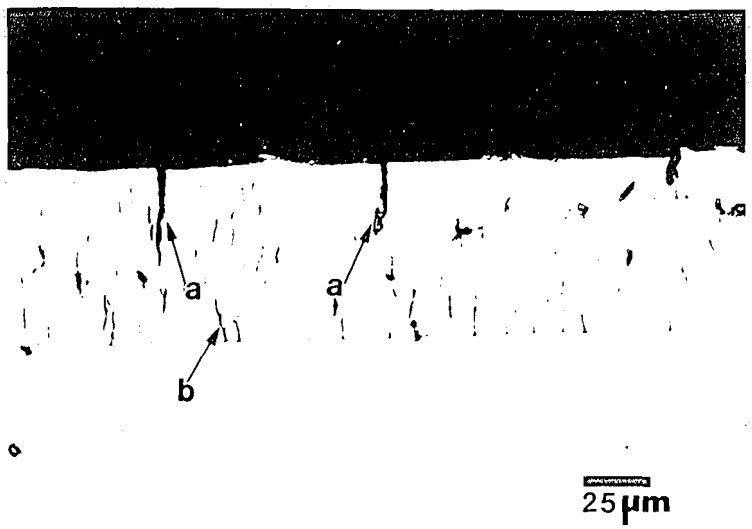

Fig. IV.30 Microstructure of the Cr layer after 100 hours of oxidation heat-treatment at 600°C. Arrows (marked a) indicate the oxidation attack at the microcracks and arrows (marked b) indicate the joining of microcracks to form larger microcracks (LOM 400X).

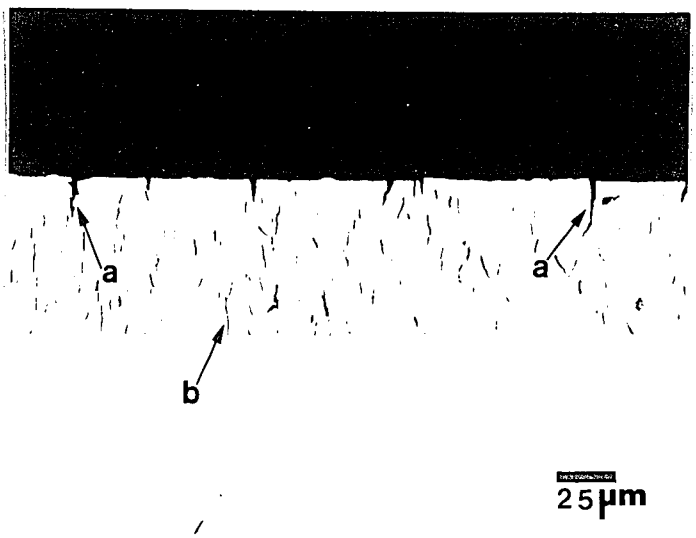

Fig. IV.31 Microstructure of the Cr layer after 250 hours of oxidation treatment at 600^{0}C. Arrows (marked a) indicate the oxidation attack at the microcracks and arrows (marked b) indicate the joining of microcracks to form larger microcracks (LOM 400X).

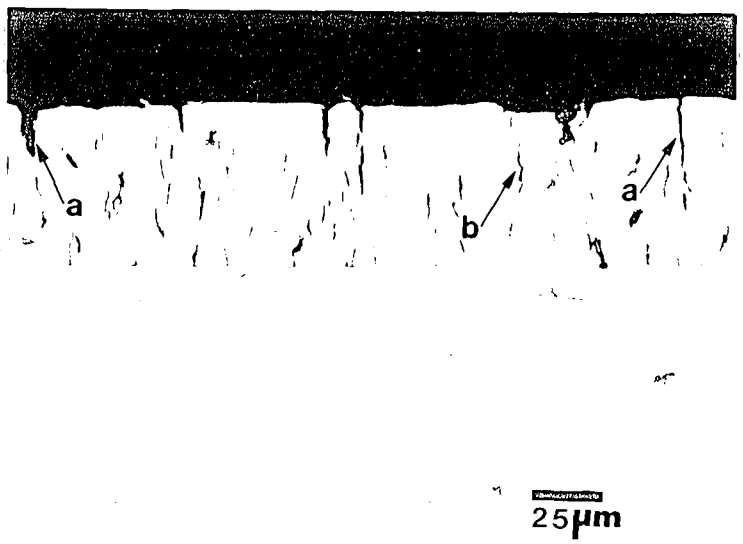

Fig. IV.32 Microstructure of the Cr layer after 500 hours of oxidation treatment at 600^{0}C. Arrows (marked a) indicate the oxidation attack at the microcracks and arrows (marked b) indicate the joining of microcracks to form larger microcracks (LOM 400X).

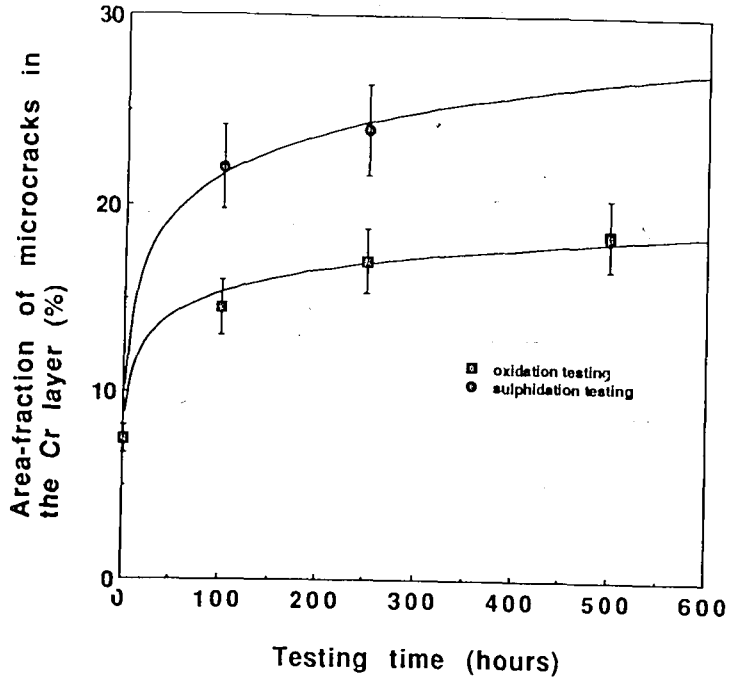

(a)

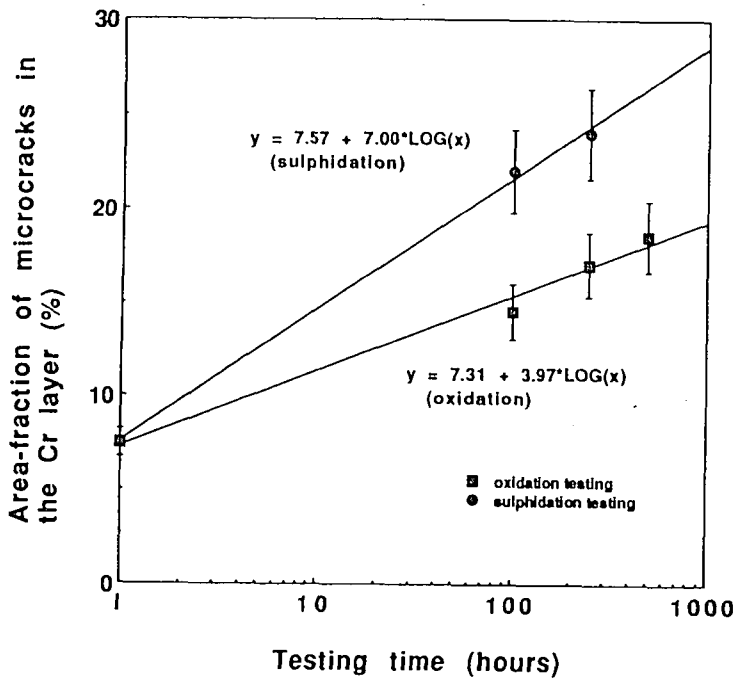

(b)

Fig. IV.33 Plot of the area fraction of microcracks in the Cr layer vs heat-treatment time in oxidation and sulphidation tests (a) Plot on a linear scale (b) Plot on a logarithmic scale.

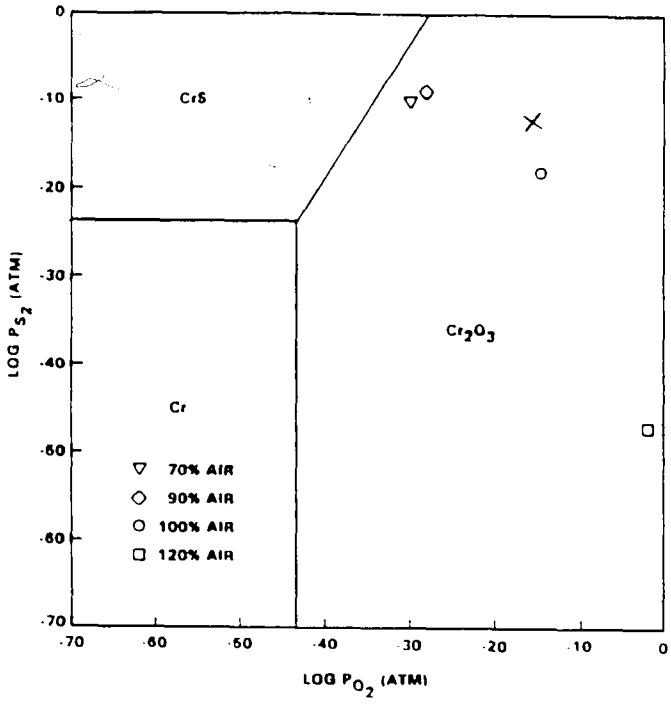

Fig. IV.34 Phase stability diagram of Cr-S-O system at 900^0F (627^0C) (reference 50)

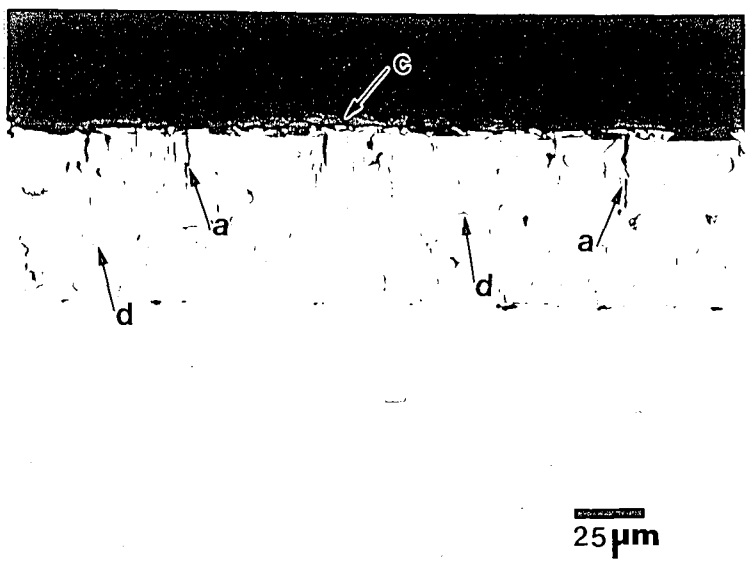

Fig. IV.35 Microstructure of the Cr layer after 100 hours of sulphidation heat-treatment at 600°C. Arrows marked (a) indicate the sulphidation attack, (c) indicate sulphidation product at the top (d) indicate lateral crack growth (LOM 400X).

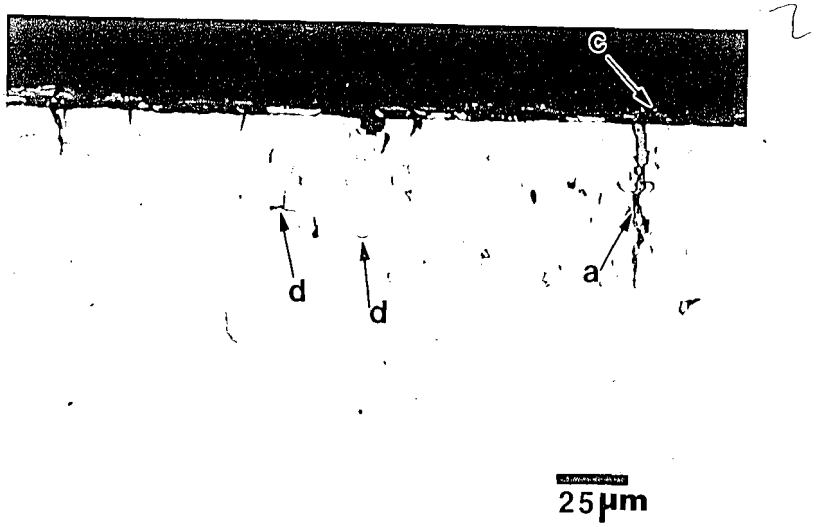

Fig. IV.36 Microstructure of the Cr layer after 250 hours of sulphidation heat-treatment at 600^{0}C. Arrows marked (a) indicate the sulphidation attack reaching the base metal (c) indicate the sulphidation product at the top and (d) indicate the lateral crack growth (LOM 400X).

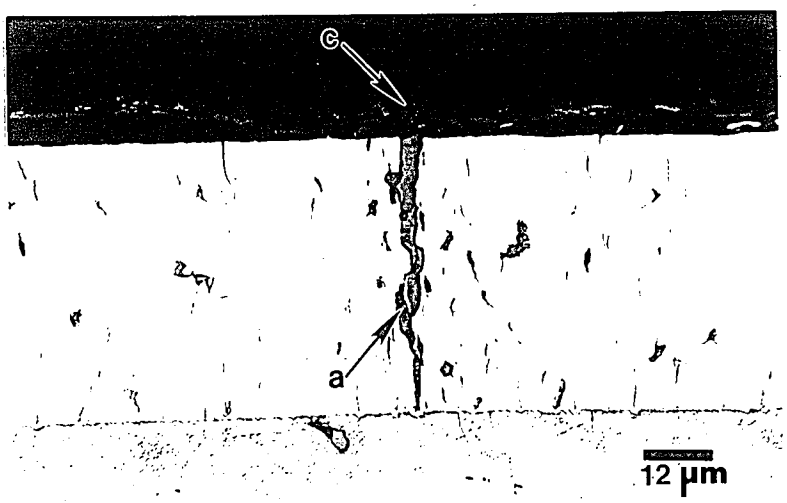

Fig. IV.37 A magnified view of the Cr layer after 250 hours of sulphidation heat-treatment at 600^{0}C. Arrow marked (a) indicates sulphidation attack at the microcracks reaching the base metal and (b) indicates the sulphidation product at the top (LOM 800X).

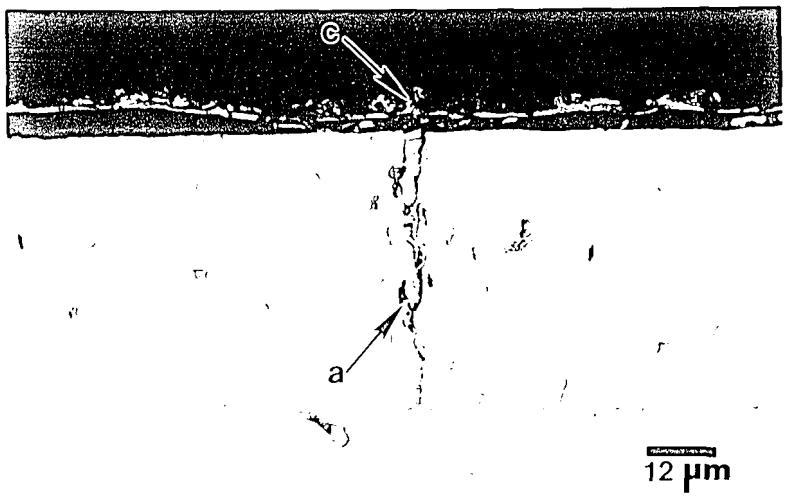

Fig. IV.37 A magnified view of the Cr layer after 250 hours of sulphidation heat-treatment at 600^{0}C. Arrow marked (a) indicates sulphidation attack at the microcracks reaching the base metal and (b) indicates the sulphidation product at the top (LOM 800X).

System	Formula	Crystal structure
C-Cr	(Cr)	bcc
	$Cr_{23}C_6$	Complex fcc, 116 atoms/unit cell a = 1.0655 nm
	Cr_7C_3	Hexagonal, 80 atoms/unit cell a = 1.401 nm, c = 0.4525 nm
	Cr_3C_2	Orthorhombic, 20 atoms/unit cell a = 1.147 nm, b = 0.5545 nm
	C	c = 0.2830 nm Hexagonal (graphitic)
Cr-Fe	(Cr)	bcc
	Sigma or FeCr	Tetragonal, 30 atoms/unit cell a = 0.8799 nm, c = 0.4544 nm

Table 1. Binary solid phases in C-Cr and Cr-Fe systems (reference 18)

Triangle	Composition (wt%) C	Cr
$\gamma Fe + M_3C + M_7C_3$		
M_3C	6.81	18.0
M_7C_3	8.61	33.2
γFe	0.53	2.50
$\gamma Fe + M_{23}C_6 + M_7C_3$		
M_7C_3	8.84	65.7
$M_{23}C_6$	5.51	51.7
γFe	0.30	10.0
$\alpha Fe + \gamma Fe + M_{23}C_6$		
$M_{23}C_6$	5.55	62.78
αFe	0.07	17.75
γFe	0.22	14.78

Table 2. Tie triangles at 870^0C (reference 20).

Element	C	Mn	P	S	Si	Ni
Wt%	0.20	<0.01	0.002	0.004	<0.01	0.01
Element	Cr	Mo	Cu	Al	Sn	Ti
Wt%	<0.01	<0.002	0.001	<0.005	<0.002	0.002

Table 3. Composition of the alloy used in the experiments (reference 28).

Time (hours)	RLT (microns)
0	0.00
100	1.40
250	2.00
500	3.30
1000	4.50
5000	9.80
10000	13.90
50000	31.10
100000	43.97

Table 4. Reaction Layer Thickness vs Time calculations.

Time (hours)	Average length (microns)	Average width (microns)
0	1.50 (0.60)	0.60 (0.20)
100 (oxidation)	4.20 (2.00)	1.45 (0.70)
250 (oxidation)	4.50 (2.10)	1.60 (0.70)
500 (oxidation)	4.55 (2.15)	1.65 (0.80)
100 (sulphidation)	2.30 (0.90)	0.90 (0.25)
250 (sulphidation)	2.35 (1.00)	0.95 (0.30)

Table 5. Variation of the average length and the average width of the microcracks as a function of time for oxidation and sulphidation tests. Numbers in the parenthesis denote the error in the measurements.

VITA

Vishal Agarwal was born to parents Narendra Agarwal and Sushma Agarwal on January 17, 1969 in Delhi, India. He received his Becholar of Technology degree in Metallurgical Engineering from the Indian Institute of Technology, Kanpur in 1991. Vishal enrolled at Lehigh University in the fall of 1991. After finishing his M.S. in Materials Science and Engineering at Lehigh, Vishal is now pursuing his Ph.D. degree at the University of Florida.

END

OF

TITLE